JOURNAL OF GEOPHYSICAL RESEARCH, VOL. 103, NO. B1, PAGES 577–596, JANUARY 10, 1998

Mineral abundance determination: Quantitative deconvolution of thermal emission spectra

Michael S. Ramsey and Philip R. Christensen
Department of Geology, Arizona State University, Tempe

Abstract. A linear retrieval (spectral deconvolution) algorithm is developed and applied to high-resolution laboratory infrared spectra of particulate mixtures and their end-members. The purpose is to place constraints on, and test the viability of, linear spectral deconvolution of high-resolution emission spectra. The effects of addition of noise, data reproducibility, particle size variation, an increasing number of minerals in the mixtures, and blind end-member input are also examined. Thermal emission spectra of 70 mineral mixtures ranging from 2 to 15 end-members and having particle diameters of 250–500 μm were obtained. Deconvolution results show that the assumption of linear mixing is valid and enables mineral percentage prediction to within 5% on average with residual errors of less than 0.1% total emissivity. One suite (21 distinct mixtures), varying from <10 μm to 500 μm, was also prepared to test the limits of the model at decreasing particle sizes. Incoherent volume scattering at grain diameters less than several times the wavelength (~60 μm) produces significant changes in spectral band morphology and hence, an increase in the root-mean-squared (RMS) error of the model. Because of this, it appears that spectral mixing remains essentially linear to ~60 μm (using the 250–500 μm size fraction as end-members). Below this threshold, the linear retrieval algorithm fails. However, with the appropriate particle diameter end-member spectra for the corresponding mixtures, the errors are reduced significantly and linearity continues through to the 10–20 μm size fraction. Additions of increasing amounts of noise cause a deviation of an additional 2.4%, whereas variability due to spectrometer reproducibility produces an average error of 4.0%. The model is also able to detect accurately minerals in mixtures containing 15 end-members, well beyond the number of geological significance. Extensive error analysis and model testing confirm the appropriateness of linear deconvolution as a useful and powerful tool to examine complexly mixed emission spectra in the laboratory and the field. The results of this study provide a foundation for remote sensing analyses of thermal infrared data from current airborne and future satellite instruments planned for Earth and Mars.

1. Introduction

The fundamental goal of remote sensing measurements, whether in the laboratory or from space, is to determine the physical and chemical characteristics of the object under study. Depending on the wavelength region examined, properties of geologic interest can include surface roughness, mineralogy, temperature, particle size, and elemental abundance. With advances in technology and the potential new applications for remote sensing, future instruments will produce extremely large data volumes, requiring faster and more accurate processing tools [*Adams et al.*, 1989].

One such data reduction technique is spectral deconvolution, which has been used for a variety of scientific problems involving mixture analyses. Using both linear and nonlinear approaches, workers have adapted the model to high-resolution visible/near-infrared (VNIR) spectra [*Johnson et al.*, 1983; *Mustard and Pieters*, 1989; *Mustard*, 1993] and to a lesser extent in the thermal infrared (TIR) portion of the electromagnetic (EM) spectrum using a linear assumption [*Thomson and Salisbury*, 1993; *Ramsey*, 1996; *Hamilton et al.*, 1997]. The fundamental principle of this technique is that the emitted or reflected energy from a multimineralic surface is a decipherable combination of the energy radiated from each component in proportion to its areal percentage. For the assumption of linearity with respect to spectral mixing, the areal percentage of surface minerals (end-members) with known particle sizes and densities translates into the volume present. If spectra of the pure end-members are known, mixture spectra can then be deconvolved through a least squares linear fit resulting in a percentage of each input end-member plus several measures of the model quality. Deconvolution provides a relatively straightforward and computationally quick method of assessing the mineral assemblages of a surface, thereby reducing hyperspectral data sets to a minimum informational volume. In addition, the products of such an analysis (areal percentage, end-members present, and model error) are easier to interpret, especially where translated into an image format, than are thermal radiance values or arbitrarily classified pixels.

The assumption of linear mixing of end-member radiant energy is not new. Early, pioneering work in laboratory reflectance and thermal emission spectroscopy led *Lyon* [1964] to suggest the possibility of linearity. Earth-based telescopic spectra [*Singer and McCord*, 1979] and multispectral data returned from the Viking lander missions to Mars were analyzed by a

Paper number 97JB02784.
0148-0227/98/97JB-02784$09.00

similar approach [*Adams et al.*, 1986]. A binary approach has been applied by *Dozier* [1981] to identify and deconvolve subpixel temperature anomalies using the two TIR bands of the advanced very high resolution radiometer (AVHRR) satellite instrument. The six VNIR spectral bands of the Landsat thematic mapper (TM) instrument have made it possible to distinguish vegetation types and monitor deforestation [*Roberts et al.*, 1990; *Adams et al.*, 1995] as well as examine eolian sand sea dynamics [*Blount et al.*, 1990] using a linear deconvolution method. More recently, mixture analysis using airborne data sets in the VNIR [*Mustard*, 1993; *Tompkins et al.*, 1997] and TIR [*Gillespie*, 1992; *Ramsey et al.*, 1993] have served as analogs for future Earth-orbiting instruments.

Much of the work to date has been done on the forward problem of spectral mixing [*Christensen et al.*, 1986; *Crown and Pieters*, 1987; *Thomson and Salisbury*, 1993], that is, performing empirical comparisons of physically mixed laboratory spectra and their numerically generated equivalents. Results from studies such as these qualitatively show that mixing in many cases appears to be linear; however, they do little to test unsupervised models, nor do they indicate the limits and errors associated with a spectral deconvolution approach. Expanding upon these comparative studies, other investigators have examined the reverse problem, that is, trying to deconvolve spectra to predict the amounts and types of minerals present and understand the geologic processes that resulted in their mixing [*Johnson et al.*, 1983, 1992; *Ramsey and Christensen*, 1992; *Sabol et al.*, 1992; *Mustard and Pieters*, 1989].

Previous workers have either concentrated on the VNIR portion of the spectrum (0.4–2.5 μm) where reflection spectra have been shown to be nonlinear upon mixing [*Nash and Conel*, 1974; *Singer*, 1981; *Clark*, 1983; *Johnson et al.*, 1992] or worked with TIR reflection [*Eastes*, 1989; *Thomson and Salisbury*, 1993], rather than emission spectra. These nonlinearities of reflected energy mixing in the VNIR can be averted to some degree by using radiative transfer equations that convert the reflection from a surface to the single scattering albedo [*Hapke*, 1981; *Mustard and Pieters*, 1989; *Johnson et al.*, 1992]. Conversions such as these do allow a linear approach to be taken, but only for a range of observation angles and particle sizes. The nonlinearities of mixing in this wavelength region were shown by *Johnson et al.* [1992], who worked with spectra of several ternary mixtures. They showed that there was no statistical chance of accurate detection of quartz for mixtures containing <30% of that mineral in olivine. To some degree this is caused by the spectrally neutral character of many silicates in the VNIR but is also a function of the overall albedo of a particular mineral. A comparison of known mineral percentages with model predicted values for another mixture suite of calcite, hypersthene, and olivine indicates a discrepancy range of 0–22% with an average close to 10% for several of the minerals [*Johnson et al.*, 1992]. An excellent summary of detection thresholds with respect to mixing analyses in the VNIR is provided by *Sabol et al.* [1992].

By comparison, the linear assumption in the thermal infrared region has been shown to be significantly more valid than in the VNIR [*Ramsey and Christensen*, 1992; *Thomson and Salisbury*, 1993]. Considering the dearth of past research in the TIR region, the need for a detailed study on the deconvolution of emission spectra becomes important considering the enormous volume of upcoming satellite data from the thermal emission spectrometer (TES) [*Christensen et al.*, 1992] instrument at Mars and the advanced spaceborne thermal emission and reflectance radiometer (ASTER) [*Kahle et al.*, 1991] planned for Earth orbit. There are several studies in the thermal infrared region with direct bearing on this effort. *Gillespie* [1992] applied an unmixing model to airborne TIR images of Death Valley, California, and was able to discriminate four end-members: vegetation, quartzite, basalt, and "virtual cold." There was no attempt to verify the model results in the field or laboratory, however. Another significant spectral mixing study in the TIR is that of *Thomson and Salisbury* [1993], who used high-resolution reflection spectroscopy to study several different mixtures at unimodal size fractions, but no attempt was made to apply a retrieval approach to the data. Rather, a forward analysis with a simple comparison of the physically mixed spectrum to the numerically mixed one showed agreements to within 5% and prompted Thomson and Salisbury to state that the assumption of linear mixing in the thermal infrared is valid.

The purpose of this study is to provide a quantitative investigation of the limits and applicability of linear deconvolution of thermal emission spectra emphasizing nonideal input conditions and evaluating the associated errors. The algorithm was applied to emission spectra of mineral mixtures of various numbers and particle sizes. Further, results were examined after the addition of random noise, the effect of spectrometer precision, and the applicability of using a blind end-member approach. A graph of the various model permutations used for this study is shown in Figure 1.

2. Theory

2.1. Visible/Near-Infrared Photon Scattering

The scattering and absorption of energy in the VNIR results in the spectral nonlinearity of mineral mixtures [*Lyon*, 1964; *Nash and Conel*, 1974; *Mustard and Pieters*, 1989]. This scattering is caused by the geometric optics of the particles with respect to wavelength together with the absorption coefficient of the minerals [*Hapke*, 1981; *Johnson et al.*, 1983; *Moersch and Christensen*, 1995]. With many minerals having a much smaller absorption coefficient, and hence a larger photon path length than the TIR region, photons undergo significantly greater volume scattering at these shorter wavelengths [*Eastes*, 1989; *Wald and Salisbury*, 1995]. Volume scattering occurs where a photon passes through one or more grains of a mixture and is incoherently scattered at every particle interface and grain asperity. Further, highly absorbing (dark) materials present in a mixture will bias the spectral features and impart a nonlinear signature on the composite spectrum [*Nash and Conel*, 1974; *Clark*, 1983]. The large probability that photons will survive passage through several transparent grains, even where those grains are much larger than the wavelength of the photon, causes weakly absorbing materials to have larger degrees of nonlinear volumetric scattering. Most geologically important rock-forming minerals such as quartz, feldspar, the aluminosilicates, and most carbonates, as well as mineral glasses, fall into this category.

2.2. Thermal Infrared Emission From Natural Surfaces

The thermal energy or radiance (L), emitted at any given wavelength (λ), is a function of the temperature of the object as well as its emissivity. Ignoring instrument effects, the blackbody radiance (B), temperature (T), and emissivity (ε) are related through the Planck equation:

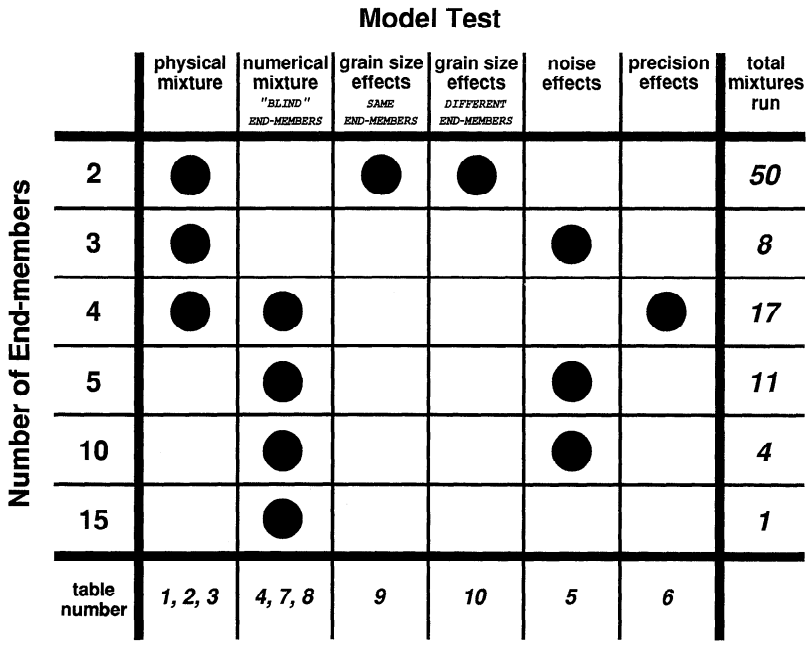

Figure 1. Deconvolution model trial matrix used for this study. Each marked box represents a different input effect tested on a given end-member suite of mineral mixtures. The total mixtures formed for a given number of end-members is shown in to rightmost column (a total of 91 mixtures were analyzed for this study). The lowermost row lists the table number corresponding to a particular model test.

$$L_{(\lambda,T)} = \varepsilon_\lambda B_{(\lambda,T)} = \varepsilon_\lambda \left\{ \frac{C_1 \lambda^{-5}}{[\exp(C_2/\lambda T) - 1]} \right\} \quad (1)$$

where $C_1 = 3.74 \times 10^{-16}$ W m^2 and $C_2 = 0.0144$ m K. An object with an emissivity value equal to unity radiates a featureless spectrum described by the Planck function and is defined as a blackbody emitter. Most materials do not behave as blackbodies, however. Rather, they have spectra with emissivity values less than one at discrete wavelengths. Commonly called absorption bands, these features are signatures of the object or mineral being analyzed. The strongest reflections occur at wavelengths corresponding to the large absorption bands or reststrahlen features, which are present in silicate and carbonate minerals [*Salisbury*, 1993; *Salisbury and Wald*, 1992]. The locations and shapes of these emission features are functions of the real and imaginary parts of the mineral's index of refraction [*Moersch and Christensen*, 1995; *Wald and Salisbury*, 1995; *Mustard and Hays*, 1997].

By comparison to the VNIR, photon/matter interaction in the thermal infrared, because of the higher absorption coefficients of the minerals, is dominated by surface or Fresnel reflections and in general combines linearly in a "checkerboard-mixing" fashion [*Gillespie*, 1992; *Adams et al.*, 1993]. In other words, the detected energy is a function of the areal percentage of the end-members present. Photons tend to interact once after being emitted/reflected from particles and therefore contain information only about that particular particle, or they are absorbed after being scattered and never reach the detector.

2.3. Spectral Variation With Particle Size

Absorption bands lessen in intensity and change in morphology with decreasing particle size; however, the positions of these features (reststrahlen bands) remain constant [*Lyon*, 1965; *Hunt and Vincent*, 1968; *Salisbury and Wald*, 1992; *Moersch and Christensen*, 1995]. It is this property that allows for identification of most geologic materials in the TIR irrespective of grain size. Significant morphological changes in spectral features due to decreasing particle size do become a factor with respect to spectral analysis well below 60 μm [*Hunt*, 1976; *Moersch and Christensen*, 1995; *Mustard and Hays*, 1997]. The position and behavior of these changes vary with wavelength and are ultimately related to the variation of the optical constants for each mineral. Explained in detail for quartz by *Moersch and Christensen* [1995] and olivine by *Mustard and Hays* [1997], the change in band shape and depth can be divided into three primary classes.

At the reststrahlen bands, which dominate vibrational spectra at large grain sizes, the mineral has a high absorption coefficient. With decreasing particle size, grains with a much larger surface area increase the potential of multiple reflections and hence the subsequent amount of energy returned to the detector (i.e., higher emissivity). In an emissivity spectrum, this scatter of emitted energy produce the linear effect of reducing the spectral contrast of the reststrahlen features (1150 cm^{-1} and 500 cm^{-1}, Figure 2).

In spectral regions where the mineral is weakly absorbing, volume transmission through the grains dominates. As particle size is decreased, more surface interfaces are created, and the potential for energy to escape the surface is reduced [*Lyon*, 1964; *Hunt and Vincent*, 1968; *Salisbury and Wald*, 1992; *Moersch and Christensen*, 1995]. In these intraband regions, emissivity decreases with grain size forming new absorption bands which continue to increase in contrast (600 cm^{-1}, Figure 2).

The third primary behavior observed in the spectra of particulates occurs in the region where the index of refraction is near unity and the absorption coefficient is rapidly increasing. At these wavelengths, very little energy is being diffracted [*Moersch and Christensen*, 1995] and the large absorption co-

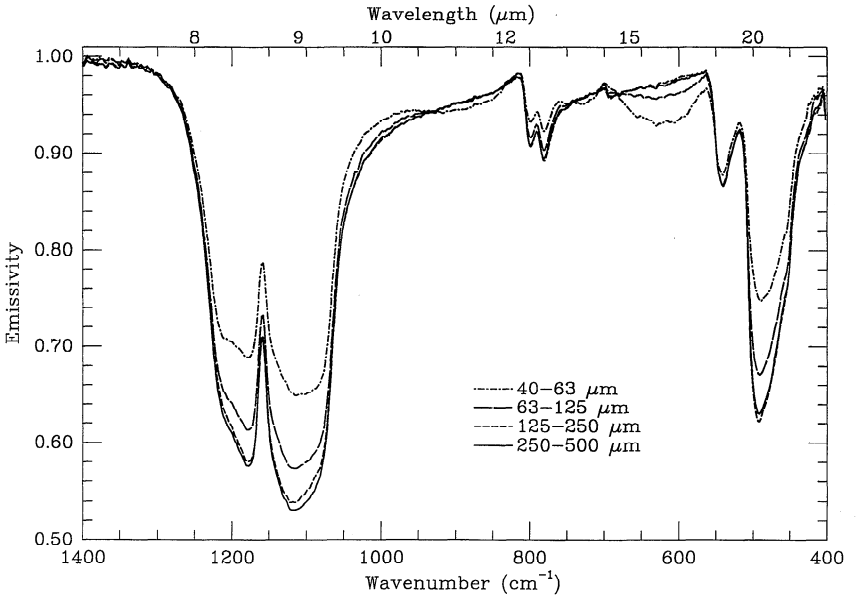

Figure 2. Effects of particle size reduction on the spectrum of quartz. As particle size is reduced, though still remaining much larger than the TIR wavelength, surface scattering is increased further due to the larger number of grain facets. These surface reflections result in more emitted energy reaching the detector, thereby decreasing the depth of the large absorption bands. Very little morphological change occurs in spectra of the largest three size fractions. The spectrum of the 40–63 μm fraction is beginning to show the effects of volume scattering of the emitted energy. The larger decrease in the depth of the reststrahlen bands as well as the nonlinear changes at 900 cm^{-1} (11.1 μm) and 650 cm^{-1} (15.4 μm) are caused by the absorption coefficient and index of refraction of quartz as emitted energy is transmitted through the volume of each grain.

efficient limits volume scattering [*Hapke*, 1993]. Known as the Christiansen feature, this region remains unaffected by changes in the grain diameter of the mineral.

Since the optical constants of the mineral are unaffected by changes in the grain diameter, the relatively large absorption coefficients and small mean optical path length for most minerals in the TIR tend to limit volume transmission to all but the smallest particles. It is this limiting of multiply-bounced photons that produces thermal emission spectra which are linear combinations of the surface minerals present and allows for the very assumption of linear deconvolution. In terms of total photons that reach a detector, a large majority have only interacted with one grain of one mineral and therefore contribute a total amount of energy to the mixed spectrum which is proportional to the areal percentage of those grains.

With further decreases in diameter to that approaching the wavelength, particles start to become optically thin to thermal infrared photons. As in the VNIR, optically thin grains allow more of the energy to pass through the particle thereby enhancing nonlinear volume scattering [*Mustard and Hays*, 1997]. Although this is not a prime concern for many terrestrial TIR remote sensing applications, the viability of linear mixing in the thermal infrared becomes questionable at grain diameters smaller than this. On Earth, very few geologic surfaces are composed of independently scattering sub-60 μm particles. Rather, in most arid and minimally vegetated regions (a prime target for future TIR remote sensing), fine-grained soil particles are commonly cemented together by chemically precipitated crusts which increase the effective radiating diameter [*Harden et al.*, 1985; *Salisbury and Wald*, 1992]. In addition to these soils, such regions typically consist of sand and coarse granual lag deposits, as well as outcrops, none of which would result in volumetric scattering [*Ramsey et al.*, 1993; *Dixon*, 1994]. Only in those rare areas of unconsolidated dust or clay would TIR spectra begin to contain scattering effects detectable to a degree that would effect the results of a linear deconvolution analysis. For Mars, there are large regions of high albedo, fine grain (<40 μm) dust [*Palluconi and Kieffer*, 1981; *Christensen*, 1986]. However, over half the planet is covered by low albedo regions composed of coarse-grained particles (200–500 μm) [*Palluconi and Kieffer*, 1981; *Christensen*, 1983] nearly identical to the size fractions used in this study. It is assumed that these areas will be the ones initially targeted for deconvolution using the approach presented here and the dusty regions necessitating a more complex (perhaps nonlinear) model.

2.4. Constrained, Least Squares Linear Retrieval Algorithm

The fundamental principle of linear mixing is that the spectral features of the end-member minerals overlap and combine in the composite spectrum in proportion to their areal fractions. This proportionality allows for a relatively simple statistical determination of the best fit end-member percentages for a given mixture spectrum [*Sabol et al.*, 1992; *Adams et al.*, 1993]. Assuming η isothermal end-members, the mathematical expression for the mixture spectrum $(\varepsilon(\lambda)_{mix})$ is stated by equation (2) with the constraint that the fractions must sum to unity:

$$\varepsilon(\lambda)_{mix} = \sum_{i=1}^{\eta} \zeta_i \varepsilon(\lambda)_i + \delta(\lambda); \qquad \sum_{i=1}^{\eta} \zeta_i = 1.0 \qquad (2)$$

where ζ_i is the areal fraction of the ith end-member $(\varepsilon(\lambda)_i)$ and is equal to the mass divided by the product of the density

and diameter. In mixtures where the particle diameters and densities for each end-member are equal, the areal percentage reduces to the mass fraction. The residual error, $\delta(\lambda)$, or model difference is calculated by subtracting the model predicted emissivity from the measured emissivity at each wavelength. This difference of the two spectra is a critical measure of the retrieval algorithm's fit and is easily visualized where displayed versus wavelength, or as an image in the case of remotely gathered data [*Gillespie et al.*, 1990; *Ramsey et al.*, 1993]. High residual errors at specific wavelengths indicate the possibility of an unmodeled absorption feature not present in either the end-member or mixture spectrum. An examination of residuals may also reveal nonlinear behavior at certain wavelengths as well as highlight areas of poor atmospheric correction and/or low instrument signal to noise (SNR). The residual error, expressed as a single value for the entire wavelength region, is known as the root-mean-square (RMS) error and determines the "goodness of fit" for a particular model iteration. For an instrument with (m) wavelength channels, this term is related to the residual error term through

$$\mathrm{RMS} = \sqrt{\sum_{j=1}^{m} \delta(\lambda)_j^2 \Big/ m} \tag{3}$$

The magnitude of the RMS varies between 0 and 1.0, with smaller values corresponding to a better fit. For example, in this study typical errors associated with high-resolution laboratory spectra were of the order of 0.10–0.010%.

Equation (2) is commonly over determined, having several unknowns (the end-member fractions and sample temperature) and hundreds of equations (the radiance measured at each wavelength). In order to solve the series of equations, the approach chosen was a numerical least squares fit using a chi-square minimization [*Ramsey*, 1996]. The technique uses a linear regression analysis, assuming a normal distribution of the data, to solve for the matrix of unknown end-member fractions [*Press et al.*, 1988]. Further, it has been shown to be the quickest computational method for manipulating large data arrays and lends itself well to the use of spectral library data sets. Remaining with the conventions used by *Press et al.* [1988] and expanding the notation to matrix form, the derivation of the chi equation reduces the solution,

$$[\zeta]_{(\eta)} = ([X]^T_{(\eta,\lambda)}[X]_{(\lambda,\eta)})^{-1}[X]^T_{(\eta,\lambda)}[U]_{(\lambda)} \tag{4}$$

where $[X]_{(\lambda,\eta)}$ is the end-member matrix of emissivity spectra at each wavelength (ε_λ) and is [λ wavelength channels by η end-members] in size. The unknown mixtue spectrum $[U]_{(\lambda)}$ can be represented as a [λ wavelength channels by 1] column vector. By assumption, each of the emissivity values in the matrix $[U]_{(\lambda)}$ is a linear combination of the emissivities from the corresponding row of the end-member matrix. The solution $[\zeta]_{(\eta)}$ is a column vector of fractions that each end-member contributes to the mixture spectra and has a length equal to the number of end-members [η end-members by 1].

This methodology allows for a maximum number of end-members equal to one plus the total number of equations or instrument wavelengths [*Sabol et al.*, 1992; *Adams et al.*, 1993]. However, because one degree of freedom is removed through the assumption of a maximum emissivity during the emissivity/temperature separation, $[\zeta]$ becomes a column vector of maximum length η. In thermal infrared remote sensing images the number of end-members is currently limited by the low number of spectral band passes of existing instruments. However, most geologic processes such as sediment mixing along an alluvial fan or within a dune field produce very few spectrally distinct end-members. Each can be easily modeled with no more than three or four end-members per scene [*Gillespie*, 1992; *Ramsey et al.*, 1993]. In addition, typical rocks will have fewer than this number of minerals in abundance. However, with the high spectral resolution of current laboratory (and future satellite) data, a much larger suite of end-members can be used if desired.

The model presented here differs from previous approaches in that the data are calibrated having the instrument terms removed, and emissivity is separated from the temperature prior to the analysis. Of the few studies using a similar deconvolution approach in the thermal infrared, all have concentrated on multispectral TIR images rather than high-resolution laboratory spectra and were applied to radiance rather than emissivity data [*Adams et al.*, 1989; *Gillespie et al.*, 1990; *Gillespie*, 1992]. By doing so, the need arises to include instrument gain and offset as well as produce an extra end-member that accounts for the temperature in the scene. Whereas this approach appears simplified, allowing for deconvolution of the image pixels without the need for further preprocessing steps, the use of radiance rather than emissivity is nonintuitive. Further, it does not apply to high-resolution laboratory data such as those presented here and does not allow for the use of a spectral library for end-members.

Because of the mathematics involved, the least squares algorithm can produce negative as well as positive values. Two constraints must be placed on the above methodology to produce results that are physically meaningful. First, if one or more of the final values of $[\zeta]$ is negative, it is presumed that the end-member corresponding to that value is not present in the mixed spectrum and is therefore removed. In other words, the model inverts the entire matrix of end-members $[X]$ and the negative end-member fractions flagged. These end-members are removed from $[X]$ and the process repeated using the new smaller $[X]$ matrix. Since negative end-members correspond to spectra that fall outside the area defined by the original end-members, these negatives are assumed not to be part of the mixture. Although this assumption causes the residual error to be slightly higher since the fit using fewer end-members is typically worse, having only positive fractional values makes for a more physically plausible solution. This constraint has been relaxed by some investigators [*Adams et al.*, 1986, 1989] and the "fraction overflow" areas used as another error analysis tool. In image format, these regions would indicate an area of a potentially unmodeled end-member.

The second constraint placed on the algorithm is that the elements of the column vector must sum to unity. The unity condition is included prior to the inversion of the end-member matrix and therefore produces fractional percentages which sum to 100%. This approach also differs from other studies which have not implemented the constraint prior to inversion of the end-member matrix. Rather, they favor the renormalization of the fractions as a final step [*Johnson et al.*, 1992]. Using the later approach can lead to a solution that can either fall short of, or sum to greater than, 100%. In doing so, the new, renormalized fractional values may not represent the most accurate solution and the associated RMS errors are typically higher.

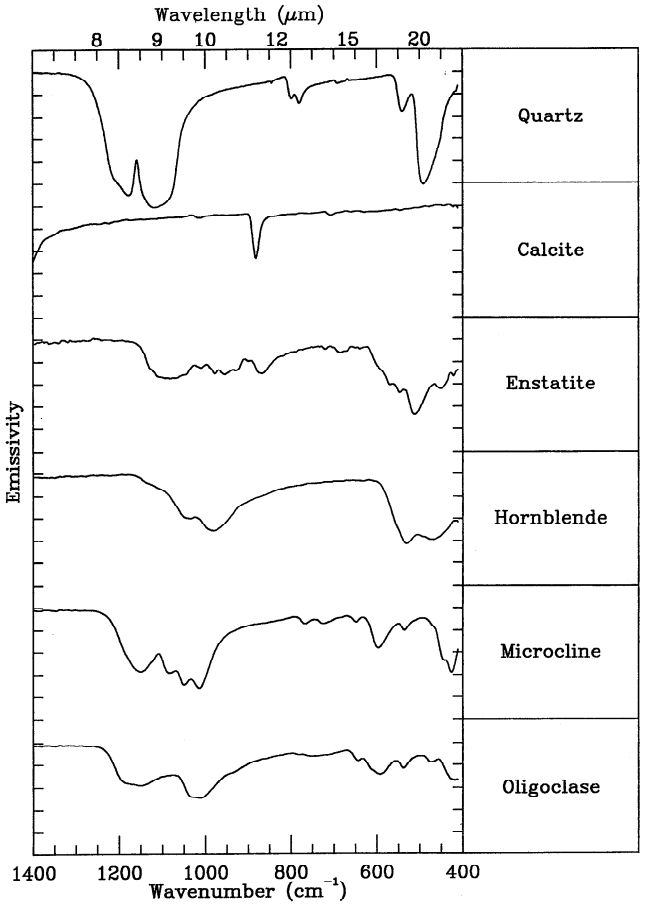

Figure 3. Emissivity spectra of 250–500 μm end-members used in the physical mixture suite. The large emissivity lows or absorption bands are caused by vibrational motions of the chemical bonds. These reststrahlen features occur at the frequencies of strongest absorption, varying from 8 to 11 μm in the silicate minerals. Each vertical tick mark represents 0.07 emissivity.

2.5. Signal to Noise Ratio

The definition of noise as it relates to spectroscopy is the ratio at a certain wavelength of the known (ideal) energy to the acquired (actual) signal. This signal to noise ratio (SNR) is inherent to the instrument and varies with wavelength and external factors such as the environment, sample alignment, and transmission of the beam splitter [*Ruff et al.*, 1997]. Typically, noise is thought of as random and having a normal distribution about the noiseless signal [*Sabol et al.*, 1992]. Although not random, it is most commonly evident in regions where atmospheric water absorption adds variability to the spectrum. These atmospheric spectral features can be minimized through controlled environmental conditions and the coaddition of spectra. However, true instrument noise is inherent in the spectral system and can vary with wavelength. For an accurate comparison of spectra gathered on different instruments under vastly different conditions, an examination of the effects of increasing noise (lowering the SNR) on the linear retrieval algorithm needs to be understood.

This was explored in great detail in a study by *Sabol et al.* [1992]. They used high-resolution laboratory spectra in the VNIR region to examine the effects on spectral mixture analysis by varying spatial scale, noise, spectral contrast of the end-members, and the reduction of the number of instrument channels. Despite the different wavelength region, their results pertaining to noise and end-member detectability limits for high resolution spectral data are of direct relevance to this study. They found that the magnitude of the detectability error was a direct function of the SNR of the mixture spectrum. For example, their confidence level for accurate detection of clay soil mixed with vegetation and shade increased from 3% to 5% as the SNR decreased from 100 to 20. The other parameters which they examined (spatial scale, instrument channels, and spectral contrast) are critical for the use of mixture deconvolution using available systems in the VNIR, but are less important for this work.

Table 1. Retrieval Model Results for the Two-End-Member Mixture Suite

Measured		Modeled		Average Model Difference, %	RMS Error, $\times 10^{-3}$
Quartz, %	Calcite, %	Quartz, %	Calcite, %		
2.00	98.00	0.51	99.49	1.49	6.250
5.00	95.00	2.39	97.61	2.61	4.866
10.00	90.00	8.09	91.91	1.91	6.471
20.00	80.00	19.68	80.32	0.32	5.101
80.00	20.00	77.03	22.97	2.97	7.149
90.00	10.00	87.58	12.42	2.42	5.712
95.00	5.00	94.09	5.91	0.91	4.395
98.00	2.00	94.43	5.57	3.57	4.060

3. Experimental Procedure

3.1. Sample Preparation

Spectra of the mineral end-members and subsequent mixtures were either obtained from crushed, sieved, and cleaned samples with well-documented petrology or culled from the TES spectral library. Mineral sample preparation consisted of several stages beginning with a detailed visual inspection of hand samples. These samples were rejected if obvious contam-

Table 2. Retrieval Model Results for the Three-End-Member Mixture Suite

Measured			Modeled			Average Model Difference, %	RMS Error, $\times 10^{-3}$
Quartz, %	Calcite, %	Enstatite, %	Quartz, %	Calcite, %	Enstatite, %		
5.00	5.00	90.00	4.25	2.60	93.14	2.10	3.270
20.00	20.00	60.00	17.67	24.18	58.15	2.79	5.781
33.00	33.00	33.00	28.66	32.16	39.18	3.78	6.797
40.00	10.00	50.00	37.86	9.27	52.87	1.92	4.572
60.00	10.00	30.00	61.00	10.50	28.49	1.01	7.296

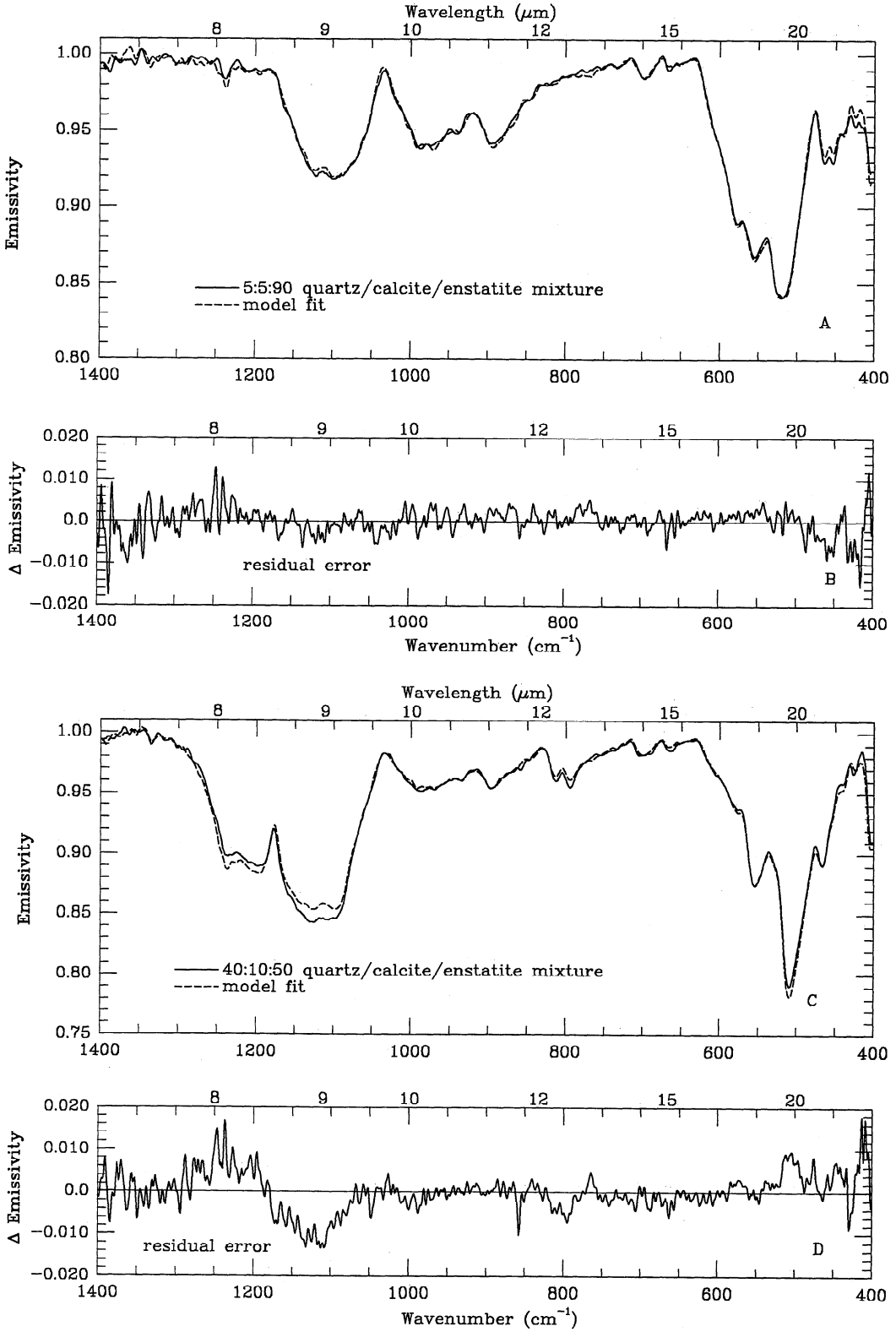

Figure 4. Emissivity spectra of the three-end-member mixtures: (a) Model results for the 5:5:90 quartz/calcite/enstatite mixture. The solid curve represents the measured spectrum, and the dashed curve represents the best model fit of the data using the end-members from Figure 3. (b) The residual error or difference between the measured and modeled spectra for this mixture. The greatest residual errors occur over the large absorption bands and in regions of atmospheric interference. (c) Model fit for the 40:10:50 mixture showing the poorer fit over the reststrahlen feature of quartz (see section 5). (d) Residual error.

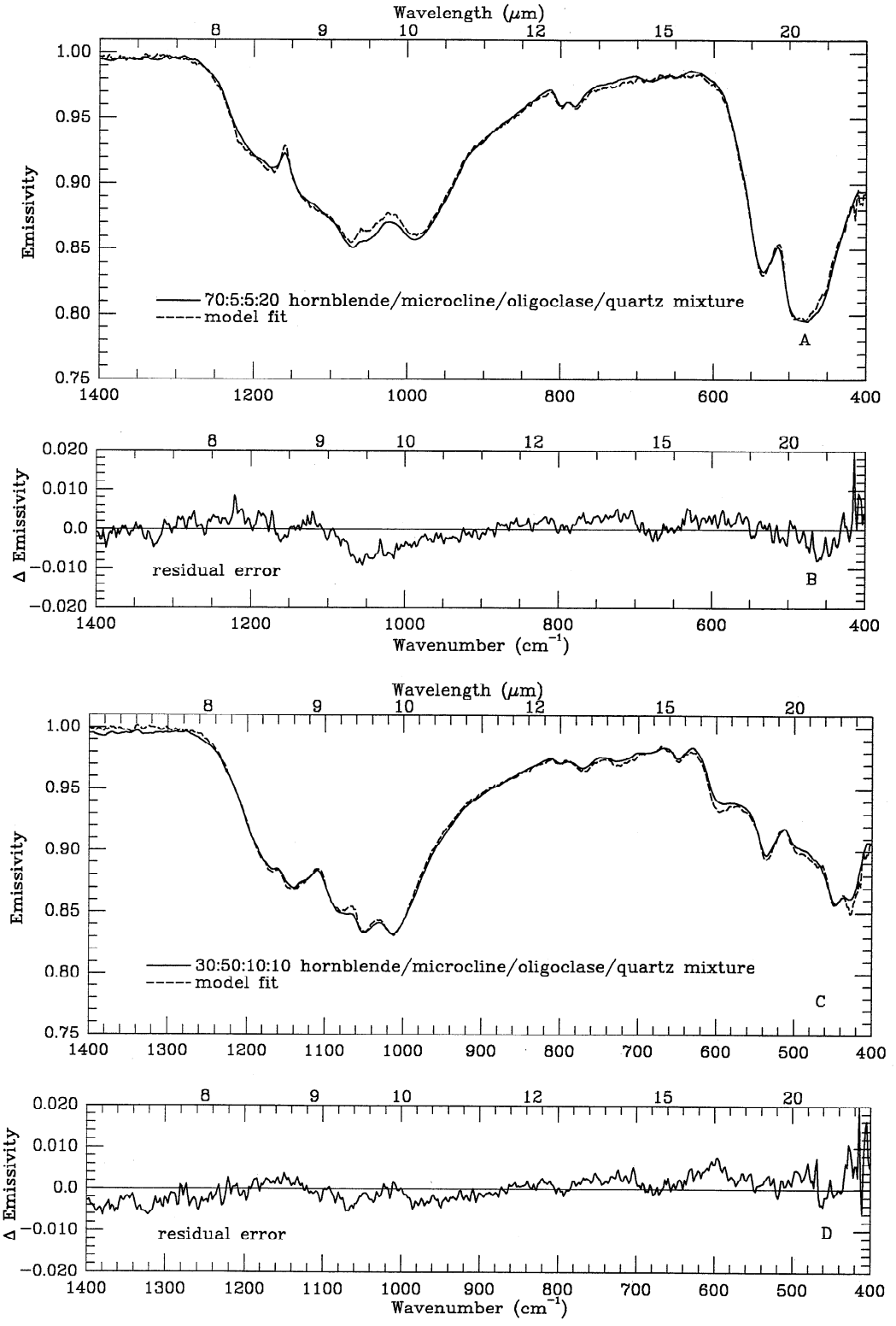

Figure 5. Model results for two of the four-component mixtures using the spectra in Figure 3 as end-members. (a) Measured spectrum and model fit for the 70:5:5:20 mixture hornblende/microcline/oligoclase/quartz with a resulting RMS error of 3.2×10^{-3}. (b) Residual error. (c) Measured spectrum and model fit for the 30:50:10:10 mixture with a similar overall fit (RMS of 3.1×10^{-3}). (d) Residual error.

inants of country rock or other mineral assemblages were detected by eye or under a magnifying hand lens. Typically, 5–10% of a bulk sample was rejected through this process. Hand samples were then crushed into centimeter-sized fragments.

Further reduction in particle size was accomplished using two techniques. The softer mineral chips were fed into a pulverizer. This process reduces particle diameters to a millimeter and below. Minerals with a hardness of quartz and above were

Table 3. Retrieval Model Results for the Four-End-Member Mixture Suite

Measured				Modeled					
Hornblende, %	Microcline, %	Oligoclase, %	Quartz, %	Hornblende, %	Microcline, %	Oligoclase, %	Quartz, %	Average Model Difference, %	RMS Error, $\times 10^{-3}$
5.00	10.00	15.00	70.00	4.31	6.02	19.27	70.40	2.34	4.776
10.00	10.00	20.00	60.00	8.41	9.66	25.31	56.62	2.65	4.308
20.00	20.00	20.00	40.00	22.16	20.32	27.59	29.94	5.03	3.928
70.00	5.00	5.00	20.00	76.47	7.80	0.00	15.73	4.64	3.235
30.00	50.00	10.00	10.00	34.56	51.88	6.85	6.72	3.22	3.191
35.00	10.00	50.00	5.00	41.09	11.48	43.42	4.01	3.78	3.420

pulverized in a tumbler/crusher device. This was deemed necessary to insure sample purity. As discussed by *Moersch* [1992], the pulverizer can deposit small (<100 μm) spherules of metallic material onto mineral grains. He postulated that where exposed to hard minerals during the crushing process, the temperature exceeded that of the metal housing of the machine. This could be observed visually in the processed quartz, which had a distinct blue-gray tint after being crushed in the pulverizer. The tumbler/crusher, on the other hand, uses pellets of "Burrundum," an artificial corrundum with a Mohs hardness of 9.5 [*Moersch*, 1992]. The device took ~6 hours to pulverize centimeter fragments of quartz into submillimeter particles.

Size sorting of the particles involved using a rototap sieve to separate grains greater than 63 μm. For all experiments in this study except one, the 250–500 μm size fraction was used for spectral acquisition and mixture construction. This size fraction was chosen for two reasons. The diameter of the particles is ~25–50 times greater than TIR wavelengths and virtually assures that no volumetric scattering will occur. As mentioned, the size fraction closely approximates that of most arid regions throughout the world and many locations on Mars.

To ascertain the effects of particle size reduction on the linear retrieval model, quartz and andesine were separated into size fractions less than 63 μm using a Stokes settling technique. This process uses graduated cylinders of deionized water and settling velocities based on particle density to divide minerals into precise size fractions. The details of the technique are described by *Moersch and Christensen* [1995]; however, the size fractions required for their study were much finer due to the nature of the radiative transfer models being tested. For this work, four relatively broad separates were prepared (<10 μm, 10–20 μm, 20–40 μm, and 40–63 μm). All mineral samples prior to spectral acquisition were washed repeatedly in alcohol to remove any fine particles clinging due to electrostatic forces [*Salisbury and Wald*, 1992].

In order to construct mixtures, mineral end-members were separated and mixed in predetermined percentages. All end-members were mixed using a mass fraction taking into account the density of each mineral (equation (2)). Several grams of the mixtures and pure end-members were each placed into specially designed copper sample cups. During the handling of a mineral sample, care was taken to minimize abrasion that would alter the known particle size distribution. The sample cups were placed in a temperature-controlled oven and allowed to equilibrate at 80°C for 24 hours.

The spectrometer's field of view of several centimeters allowed the entire sample surface to be detected. However, to guarantee accurate exposure of the mineral grains in proportion to the mixed percentage, the sample surface was remixed several times and new measurements made. The average of these measurements was used as the final composite spectrum for the deconvolution analysis. Typical variations in the spectra were less than 2%, falling within the range of the spectrometer's precision and indicating that the correct percentages were consistently being detected.

3.2. Instrumentation and Spectral Acquisition

All thermal infrared spectra for the mineral samples were acquired in emission using a Mattson Cygnus 100 interferometric spectrometer (for a detailed instrument description, see *Barbera* [1989], *Christensen and Harrison* [1993], and *Ruff et al.* [1997]). The spectral wavelength region sampled is approximately 6.6 to 25 μm (1500–400 cm^{-1}), which includes the

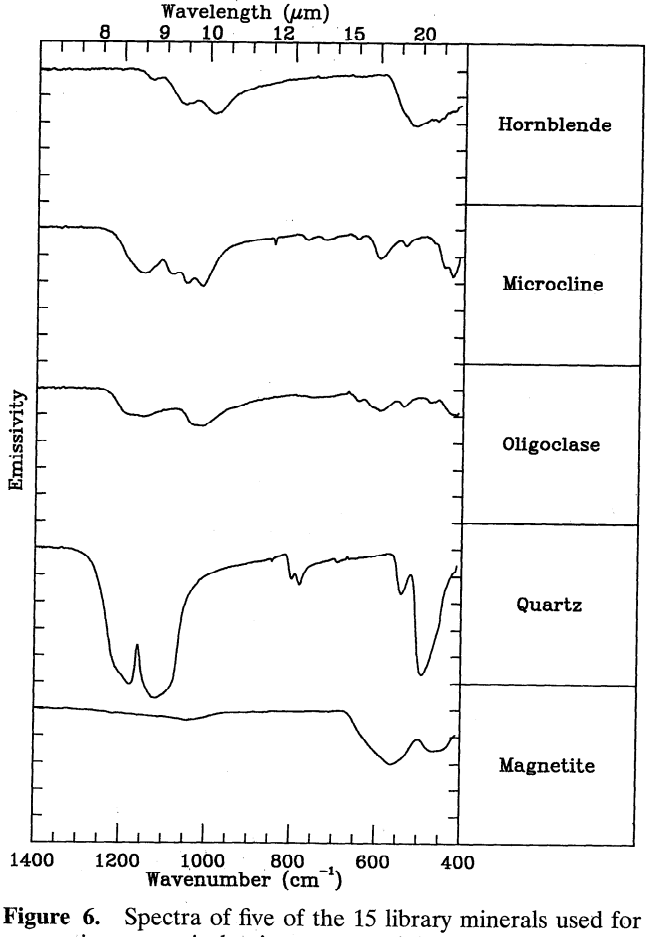

Figure 6. Spectra of five of the 15 library minerals used for generating numerical mixtures containing greater than five end-members. Each vertical tick mark represents 0.08 emissivity.

Table 4a. Blind Retrieval Results (Using 10 End-Members) for Five-Component Numerical Mixture of 25% Enstatite, 10% Hornblende, 30% Augite, 25% Oligoclase, and 10% Magnetite With Additive Noise

End-Member	Measured, %	Modeled, %				Model Difference, %
		0% Noise	10% Noise	20% Noise	30% Noise	30% Noise
Enstatite	25.00	25.05	26.11	27.40	29.06	4.06
Hornblende	10.00	9.98	10.47	11.04	11.78	1.78
Gypsum	0.00	0.00	0.00	0.00	0.00	0
Augite	30.00	29.95	28.25	26.09	23.32	6.68
Calcite	0.00	0.00	0.00	0.00	0.00	0
Microcline	0.00	0.00	0.00	0.00	0.00	0
Oligoclase	25.00	25.00	24.75	24.43	24.01	0.99
Quartz	0.00	0.00	0.00	0.00	0.00	0
Montmorillonite	0.00	0.00	0.59	1.35	2.33	2.33
Magnetite	10.00	9.98	9.76	9.47	9.09	0.91
RMS error	···	4.390E−04	1.586E−03	3.489E−03	5.954E−03	···

Read 4.390E−04 as 4.390×10^{-4}.

diagnostic vibrational features of most rock-forming minerals. The instrument has a spectral sampling of 2 cm^{-1} over the entire wavelength region with a SNR ratio approaching 500 over the highest sensitivity of the spectrometer (8–20 μm). Atmospheric interference due to water vapor at wavelengths short of 8 μm and carbon dioxide at wavelengths longer than 12 μm is minimized by a constant nitrogen purge of the spectrometer and sample chamber. However, even under the most ideal situations, small amounts of water vapor are visible as minor absorption bands in the spectra (Figure 2). Each spectral measurement takes ~2 s to acquire, and to attain the highest possible signal to noise ratio, anywhere from 64 to 200 individual spectra per sample were averaged. This averaged spectrum constituted one sample measurement. As mentioned, in order to minimize errors associated with a preferred arrangement of the grains in the holder, samples were then remixed and new spectra were acquired.

The derivation of calibrated, absolute emissivity [*Christensen and Harrison*, 1993; *Salisbury et al.*, 1994] is much more difficult than the simple ratio of equation (1). To calibrate a spectrometer and determine the absolute emissivity in the TIR accurately, factors such as the instrument response function, atmospheric interference, instrument energy, and reflected energy from the environment all have to be taken into account. The emissivity of the sample as a function of wavelength can be described by the one temperature method of *Christensen and Harrison* [1993],

$$\varepsilon_s = \frac{\left\{\dfrac{[V_{s(T)} - V_{bb(T_w)}]}{[V_{bb(T_h)} - V_{bb(T_w)}]}\right\}[B_{bb(T_h)} - B_{bb(T_w)}] + B_{bb(T_w)} - B_{env(T)}}{[B_{s(T)} - B_{env(T)}]} \quad (5)$$

where V_s and V_{bb} are the voltages measured by the spectrometer for the sample and blackbody, respectively. B is the radiance determined from solution of the Planck equation evaluated at the measured environmental, hot, and warm blackbody temperatures [env(T), bb(T_h), and bb(T_w)]. The fundamental assumption in the derivation of emissivity using only one sample measurement is that the environmental energy reflected from the sample follows Kirchoff's law and is thus one minus the emissivity [*Salisbury et al.*, 1994]. Because this reflected term is a second-order effect, the assumption contributes very little error into the calculation of absolute emissivity [*Ruff et al.*, 1997]. The primary advantages of using the one temperature technique are speed (only one spectral acquisition per sample) and a higher SNR (less noise introduced into the equation via another spectrum of the sample measured at another temperature).

In studies using the Mattson spectrometer and the various methods of deriving emissivity, *Ruff et al.* [1997] have per-

Table 4b. Blind Retrieval Results (Using 10 End-Members) for Five-Component Numerical Mixture of 10% Hornblende, 25% Microcline, 20% Oligoclase, 40% Quartz, and 5% Magnetite With Additive Noise

End-Member	Measured, %	Modeled, %				Model Difference, %
		0% Noise	10% Noise	20% Noise	30% Noise	30% Noise
Enstatite	0.00	0.00	0.00	0.00	0.00	0
Hornblende	10.00	9.93	9.71	9.34	8.88	1.12
Gypsum	0.00	0.00	0.00	0.00	0.00	0
Augite	0.00	0.09	0.00	0.00	0.00	0
Calcite	0.00	0.00	0.00	0.00	0.00	0
Microcline	25.00	24.97	25.48	26.08	26.84	1.84
Oligoclase	20.00	20.01	19.40	18.62	17.62	2.38
Quartz	40.00	40.00	39.53	38.95	38.20	1.8
Montmorillonite	0.00	0.00	1.17	2.65	4.55	4.55
Magnetite	5.00	4.99	4.55	3.99	3.28	1.72
RMS error	···	6.500E−05	1.443E−03	3.241E−03	5.554E−03	···

Read 6.500E−05 as 6.500×10^{-5}.

Table 4c. Blind Retrieval Results (Using 10 End-Members) for Five-Component Numerical Mixture of 20% Hornblende, 20% Calcite, 20% Microcline, 20% Quartz, and 20% Montmorillonite With Additive Noise

End-Member	Measured, %	Modeled, %				Model Difference, % 30% Noise
		0% Noise	10% Noise	20% Noise	30% Noise	
Enstatite	0.00	0.00	0.00	0.00	0.00	0
Hornblende	0.00	0.00	0.00	0.00	0.00	0
Gypsum	20.00	20.00	19.61	19.13	18.50	1.5
Augite	0.00	0.00	0.00	0.00	0.00	0
Calcite	20.00	20.00	19.82	19.60	19.32	0.68
Microcline	20.00	19.99	20.17	20.38	20.66	0.66
Oligoclase	0.00	0.00	0.00	0.00	0.00	0
Quartz	20.00	20.00	19.64	19.20	18.63	1.37
Montmorillonite	20.00	20.01	20.61	21.36	22.32	2.32
Magnetite	0.00	0.00	0.00	0.00	0.00	0
RMS error	...	2.300E−05	1.458E−03	3.280E−03	5.623E−03	...

Read 2.300E−05 as 2.300×10^{-5}.

formed a detailed error analysis for all contributing factors and report an instrument precision, and thus an overall spectral reproducibility, of 0.5%. This value is a great improvement over past years due to significant enhancements in the spectrometer and acquisition technique. Spectra used in this study were gathered over the course of these improvements and therefore could have inherent instrument errors that range from 0.5% to approaching 4.0% (the larger values being associated with repeat measurements over time). However, because spectra of a given mineral mixture suite and its end-members were always acquired on the same day, it is unlikely that reproducibility errors of 4% were encountered even in the oldest spectral measurements. This factor is the primary cause of the minor variations in the spectral features of a mineral as compared to its counterpart from a different mixture suite. However, all spectra belonging to an individual suite acquired on the same day had no variations or noise differences between end-member and mixture.

4. Results

4.1. Increasing the Number of End-Members

A binary mixing suite of quartz and calcite was prepared as the first physical test of the linear retrieval algorithm. The primary goal of this initial test was to examine the detection limits of the algorithm and spectrometer. For this reason, mixture percentages are concentrated on the low (0–20%) and high (80–100%) ends of the possible range. The strong absorption band of calcite (~1500 cm^{-1}) and the doublet of quartz (~1150 cm^{-1}) are the main reststrahlen features of these minerals. The crystal structures of both are rather simple, which is reflected by the few and well-defined absorption features in each spectrum. The spectra of the particulate end-members are shown in Figure 3 and the results of the model are given in Table 1. The results indicate an average model difference in predicted percentage of 2.0% with and average RMS error of 0.55% [*Ramsey and Christensen*, 1992].

The number of mineral end-members was increased by one with the addition of enstatite (Figure 3). The change from a framework arrangement of silica tetrahedra in quartz to the more loosely bound chain structure in enstatite is evident upon comparison of the two spectra. The strong reststrahlen feature in quartz is broadened, shallowed, and shifted to longer wavelengths (lower vibration frequencies). The results for the three-end-member suite are listed in Table 2 and are similar to those of the quartz/calcite mixtures. The modeled percentage errors range from 0.5% to 6.2% with an average of 2.3% and an average RMS error of 0.55%. Figure 4 shows the measured spectra and model results for two of the quartz/calcite/enstatite mixtures. The residual error is the emissivity difference between the two spectra and is positive over wavelength regions where the measured spectrum is shallower than the modeled. The good alignment of the modeled spectra with the actual measurements is evident in the small residual errors (less than

Table 4d. Blind Retrieval Results (Using 10 End-Members) for 10-Component Numerical Mixtures With Additive Noise

End-Member	Measured, %	Modeled, %				Model Difference, % 30% Noise
		0% Noise	10% Noise	20% Noise	30% Noise	
Enstatite	10.00	9.91	11.42	13.30	15.73	5.73
Hornblende	10.00	10.03	9.80	9.53	9.17	0.83
Gypsum	10.00	9.99	9.53	8.69	8.23	1.77
Augite	10.00	10.05	8.07	5.59	2.39	7.61
Calcite	10.00	10.00	9.41	8.66	7.71	2.29
Microcline	10.00	9.94	8.91	7.61	5.94	4.06
Oligoclase	10.00	10.06	10.89	11.92	13.26	3.26
Quartz	10.00	10.00	9.54	8.96	8.21	1.79
Montmorillonite	10.00	10.02	13.08	16.90	21.81	11.81
Magnetite	10.00	9.98	9.12	8.05	6.67	3.33
RMS error	...	1.680E−04	1.367E−03	3.056E−03	5.231E−03	...

Read 1.680E−04 as 1.680×10^{-4}.

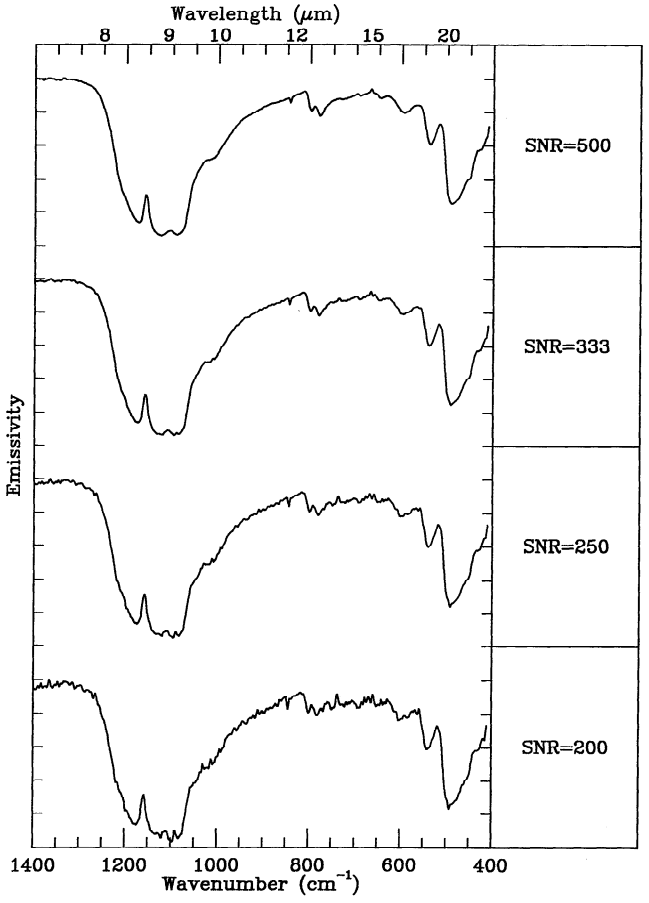

Figure 7. Numerically generated spectra of 10:25:20:40:5 mixture of hornblende/microcline/oligoclase/quartz/magnetite (top) with a decreasing signal to noise (SNR) ratio. The simulated reduction in the spectrometer's SNR through addition of random noise obscures the finer spectral features of the original mixture. This addition produced an average error in the model predicted percentage of 1.34% with an increase in the RMS error (5.5×10^{-3}). Each vertical tick mark represents 0.06 emissivity.

1.0%), indicating the strong linear relationship between areal fraction and the depth and morphology of the spectral features.

Hornblende, microcline, oligoclase, and quartz (Figure 3) were mixed to produce end-member mixtures (Figure 5). This new mineral suite was chosen to mimic the compositions of granitic and granodioritic rocks. The same procedure of mixture construction, spectral acquisition, and model application was performed with the results listed in Table 3. The predicted percentage had an error range of 0.3–10.1%, with an average of 3.6%, slightly higher than the initial results. However, the average RMS error (0.38%) for the entire suite decreased from previous mixtures. This increase in model fit is attributed to better spectral calibration and the use of minerals with less pronounced spectral contrast between features. Figure 5 shows the model fits for the 70:5:5:20 and the 30:50:10:10 mixtures of hornblende/microcline/oligoclase/quartz. The largest residual error occurs at 1050 cm^{-1} (9.5 μm) in Figure 5b, corresponding to the maximum spectral contrast between quartz and hornblende. RMS errors for the entire spectrum are <0.5% for both mixtures, indicating the dominance of linear mixing.

For mixtures with greater numbers of end-members, the TES spectral library was sampled. Spectra of 15 minerals (Figure 6) were used to form numerical, rather than physical, mixtures. This was done to limit sample preparation time and was based on the success of the model thus far. In addition, the spectra of these mixtures were subjected to the effect of increased noise using a blind end-member approach to determine the model sensitivity. The need for physical mixtures containing 10 or more end-members becomes far less critical for these types of studies.

4.2. Additive Noise

The introduction of noise for this purpose was accomplished by generating a random noise pattern with a total emissivity variation of ±1%. This noise spectrum was then convolved with the spectra of real and numerical mixtures in increments which translated into a lowering of the spectrometer SNR from 500 to 200. The new "noisy" spectra were then deconvolved using their original end-members. This approach is similar to that of *Sabol et al.* [1992], who examined the effects of noise on existing VNIR instruments.

Four mixtures were numerically created from the mineral end-members (Figure 6) taken from the spectral library and composited with the noise spectrum. The first three mixtures used five end-members and the last represents a 10-end-member composite. The minerals, percentages, and results of the deconvolution are listed in Table 4, and spectra of one of the mixtures are shown in Figure 7. This mixture of 10:25:20:40:5 hornblende/microcline/oligoclase/quartz/magnetite resulted in variations in the predicted end-member percentages from a minimum of 0.6% to a maximum of 11.8% with decreasing the SNR (Figure 8). In addition, as the noise was increased, the loss of small-scale spectral features produced

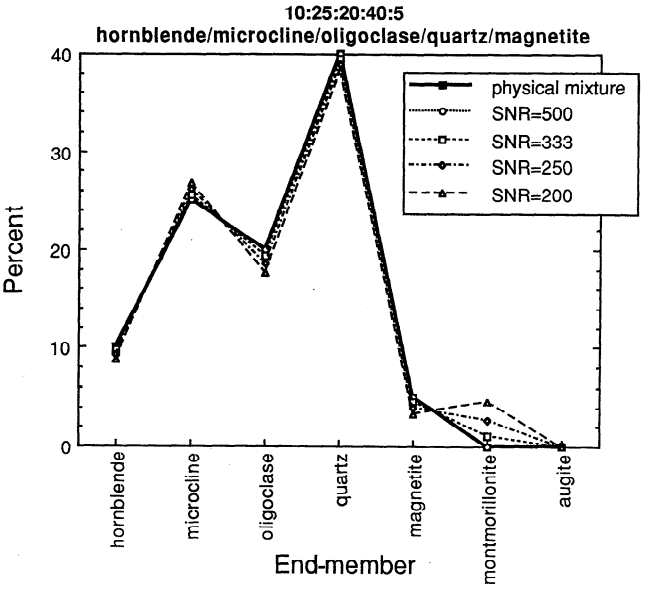

Figure 8. Variation in the retrieval algorithm's modeled percentages as a function of the lower SNR for the mixture displayed in Figure 7. The addition of noise to the spectra of the mixtures can generate errors as large as 11.8% in the predicted areal end-member fractions; however, the average for all the mixtures subjected to noise was 1.98%. Note also the prediction of augite and montmorillonite, which were not present in the original mixture (see text).

Table 5. Model Results for the Three-End-Member Mixture of 40:10:50 Quartz/Calcite/Enstatite With Increasing Additive Noise

End-Member	Quartz, %	Calcite, %	Enstatite, %	RMS Error, $\times 10^{-3}$
Measured	40.00	10.00	50.00	...
0% noise	37.89	9.38	53.07	4.572
10% noise	37.33	9.7	53.16	4.386
20% noise	36.62	10.11	53.28	4.951
30% noise	35.71	10.62	53.42	6.268

the spurious result of sodium montmorillonite to be predicted in a statistically significant quantity by the model. In general, however, the model errors averaged over the number of mineral end-members for each mixture were only 1.68%, 1.34%, 0.65%, and 4.25% for the three five-end-member and one 10-end-member mixture, respectively. These errors yield an average of 1.98% for a greater than 50% decrease in SNR.

The 40:10:50 mixture (Figure 4c) from the quartz/calcite/enstatite suite was chosen as a representative physically mixed example, and the results of increasing noise on this spectrum using the model are presented in Table 5. The addition of noise produced an average deviation of 2.78% in the retrieval results, with an increase in the RMS error from 4.5×10^{-3} to 6.3×10^{-3}. The higher error in the physically mixed example can be attributed to the slight nonlinearities over the reststrahlen features and yet is still remarkably small considering the degree of spectral degradation. Further, the average model error of 2.4% for all the mixtures subject to noise falls within the spectral variability of the instrument.

4.3. Spectral Precision

The precision of the spectrometer is the variation in emissivity of repeat measurements of the same sample. After calibration of the measured radiance and the derivation of emissivity, this precision error is typically manifested as a variation in spectral depth of large emission features. The absolute precision value of any spectrometer is the fundamental limiting certainty that any spectral fitting algorithm can guarantee accurate results. Because such routines rely on the morphology of absorption features, changes in their depth due to reproducibility factors will have an affect on the output of such models. As mentioned, improvements to the current laboratory spectrometer have reduced this figure from 3–4% to less than 0.5% currently. Some of the spectra used in this study were acquired prior to many of these improvements and were therefore subject to the higher errors. However, the largest errors in precision result from instrument drift due to changing external conditions (most notably over the course of many days). Since both end-member and mixture data were always acquired on the same day, this error is reduced significantly and is assumed to be less than 2%.

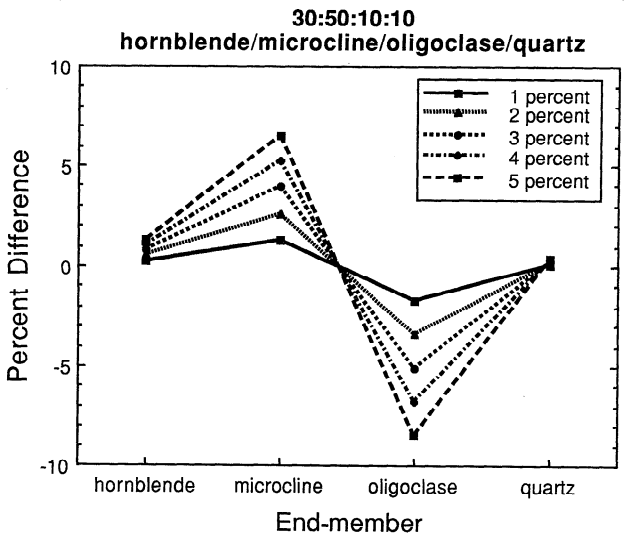

Figure 9. Model errors with spectrometer precision using the 30:50:10:10 physical mixture (Figure 5c) of hornblende/microcline/oligoclase/quartz end-members. A maximum error range of up to 5% precision is shown. However, current estimates place this error closer to 0.5% (see text). Changes in the spectral band depth directly translate into percentage errors of the retrieval algorithm's results. An average error of 4% due to a spectrometer variability of 5% indicates the approximate linearity of the model with instrument precision.

Subjected to the deconvolution analysis, spectra with a simulated variability of 2% (±1%) produced errors of 0.5–4.0% (Table 6). The same procedure was repeated for increasing precision errors of 1–5% (Figure 9). The average model error was 4.0% indicating an approximate linear relationship of reproducibility and deconvolution.

4.4. Blind End-Member Input

If the retrieval algorithm is only given the spectral end-members of exactly the minerals that form the unknown spectrum, it is "forced" to fit those particular minerals. As is the case for all remote sensing applications and many laboratory samples, the exact composition of the sample is not known. In fact, the ability to determine composition is one of the fundamental objectives of a linear retrieval approach. To accomplish this, an entire spectral library, or logically narrowed subset thereof, should be used as possible end-members. Known as

Table 6. Retrieval Model Results for a Four-End-Member Mixture With Decreasing Spectral Precision

End-Member	Hornblende, %	Microcline, %	Oligoclase, %	Quartz, %	RMS Error, $\times 10^{-3}$
Measured	30.00	50.00	10.00	10.00	...
0% variation	34.56	51.88	6.85	6.72	3.191
1% variation	34.52	50.90	8.58	6.68	3.159
2% variation	34.25	49.59	10.27	6.61	3.160
3% variation	33.99	48.28	11.96	6.53	3.196
4% variation	33.73	46.95	13.65	6.46	3.262
5% variation	33.46	45.67	15.34	6.38	3.405

Table 7. Blind Retrieval Results for the 15-End-Member Numerical Mixture

End-Member	Measured, %	Modeled, %	Model Difference, %
Enstatite	20.00	19.69	0.31
Hornblende	10.00	9.77	0.23
Gypsum	10.00	9.85	0.15
Augite	10.00	9.08	0.92
Calcite	5.00	5.04	0.04
Microcline	5.00	4.97	0.03
Oligoclase	5.00	5.01	0.01
Quartz	5.00	5.02	0.02
Montmorillonite	5.00	5.00	0
Magnetite	5.00	4.84	0.16
Kyanite	4.00	4.05	0.05
Pyrophyllite	4.00	4.01	0.01
Tourmaline	4.00	4.09	0.09
Diopside	4.00	5.22	1.22
Forsterite	4.00	4.06	0.06
RMS error, $\times 10^{-3}$	...	2.728	...

blind end-member input, this allows the model to find the best fitting combination of minerals.

For the purpose of these initial trials, the numerical and physical mixtures were subjected to this blind approach allowing the model to choose from the 15-end-member suite of possible minerals. The 5-, 10-, and 15-end-member mixtures (numerically generated with decreasing SNR) as well as the four-end-member physical mixture were deconvolved and the results presented in Tables 4, 7, and 8. In the case of the numerically mixed noisy spectra the correct end-members were consistently chosen with the exception of the lowest SNR, in which several minerals were chosen that were not part of the composite spectrum (Table 4). However, these modeled end-members were consistently below 5% and only present in the lowest SNR spectra. Because this mixture was numerically generated, the accuracy of the modeled percentages is likely exaggerated, however. The results for the physical mixture of hornblende/microcline/oligoclase/quartz were similar with respect to the accurate identification of the end-member minerals. Comparison of the actual percentages shows a deviation of as much as 12%, but an average error for all the end-members of only 3.47% (Table 8).

4.5. Particle Size Variation

The effects on linear deconvolution of reducing particle diameters were investigated in one binary suite of quartz and andesine. The significant changes in absorption band morphology as volume scattering becomes a dominant component of the emitted energy can be seen for quartz and andesine in Figure 10. For silicate minerals, these changes generally become evident at the 40–63 μm grain size fraction [*Salisbury and Wald*, 1992; *Moersch and Christensen*, 1995; *Mustard and Hays*, 1997].

Two approaches were taken in application of the model to this spectral suite. First, assuming a future spectral library will have minerals composed of only one grain size, the algorithm was run using the 250–500 μm end-member on the entire size fraction of mixed spectra. The goal of this phase was to determine accurately where linear deconvolution fails regardless of particle size. Second, by applying the same methodology only using the end-member spectra from each size fraction to deconvolve the corresponding mixed spectrum, features arising from size effects could then be modeled. This analysis will have an impact on whether future libraries should contain spectra of mineral size suites as well.

Because of the insignificant changes of the end-member spectra having diameters greater than 63 μm, the results of linear deconvolution of these size fractions with the 250–500 μm end-member showed little difference (Tables 9 and 10). As expected, below this threshold, the model can no longer accurately fit mixture spectra. Figure 11a shows the results of the retrieval algorithm for the 10–20 μm mixture of 50:50 quartz/andesine. With a large RMS of 2.43% and a predicted areal percentage of 10:90, the model is obviously invalid. Since the chosen end-member spectra contain no features due to volume scattering, these spectral regions contain the largest residual errors. However, with spectra of the correctly sized end-members, the model results improve to a predicted end-member percentage of 44:56 quartz/andesine and a residual error of 1.09×10^{-3} (Figure 11b). These results for each of the three mixture ratios are graphically represented in Figure 12 as

Table 8. Blind Retrieval Results Using 15 End-Members for the Physical Mixtures of Hornblende/Microcline/Oligoclase/Quartz

End-Member	Measured, %	Modeled, %	Measured, %	Modeled, %	Measured, %	Modeled, %	Measured, %	Modeled, %	Measured, %	Modeled, %	Measured, %	Modeled, %
Enstatite	...	...	...	...	...	...	...	...	...	...	...	...
Hornblende	5.00	1.51	10.00	7.66	20.00	18.98	70.00	67.93	30.00	27.75	30.00	32.57
Gypsum	...	...	...	...	...	...	...	...	...	...	...	...
Augite	...	...	...	...	...	...	...	2.11	...	...	...	2.94
Calcite	...	...	...	...	...	...	...	...	...	...	...	...
Microcline	10.00	11.28	10.00	21.99	20.00	31.20	5.00	6.16	50.00	53.04	10.00	11.59
Oligoclase	5.00	6.80	20.00	13.44	20.00	10.50	5.00	...	10.00	7.47	50.00	44.35
Quartz	80.00	79.68	60.00	56.93	40.00	36.62	20.00	19.16	10.00	8.74	5.00	8.45
Montmorillonite	...	...	...	...	...	...	...	...	...	...	...	...
Magnetite	...	...	...	...	...	...	...	...	...	...	...	...
Kyanite	...	...	...	...	...	...	...	...	...	...	...	...
Pyrophyllite	...	...	...	...	...	2.71	...	4.65	...	3.00	...	0.09
Tourmaline	...	...	...	...	...	...	...	...	...	...	...	...
Diopside	...	...	...	...	...	...	...	...	...	...	...	...
Forsterite	...	...	...	...	...	...	...	...	...	...	...	...
RMS error, $\times 10^{-2}$	...	3.592	...	2.970	...	2.213	...	1.842	...	1.556	...	1.468

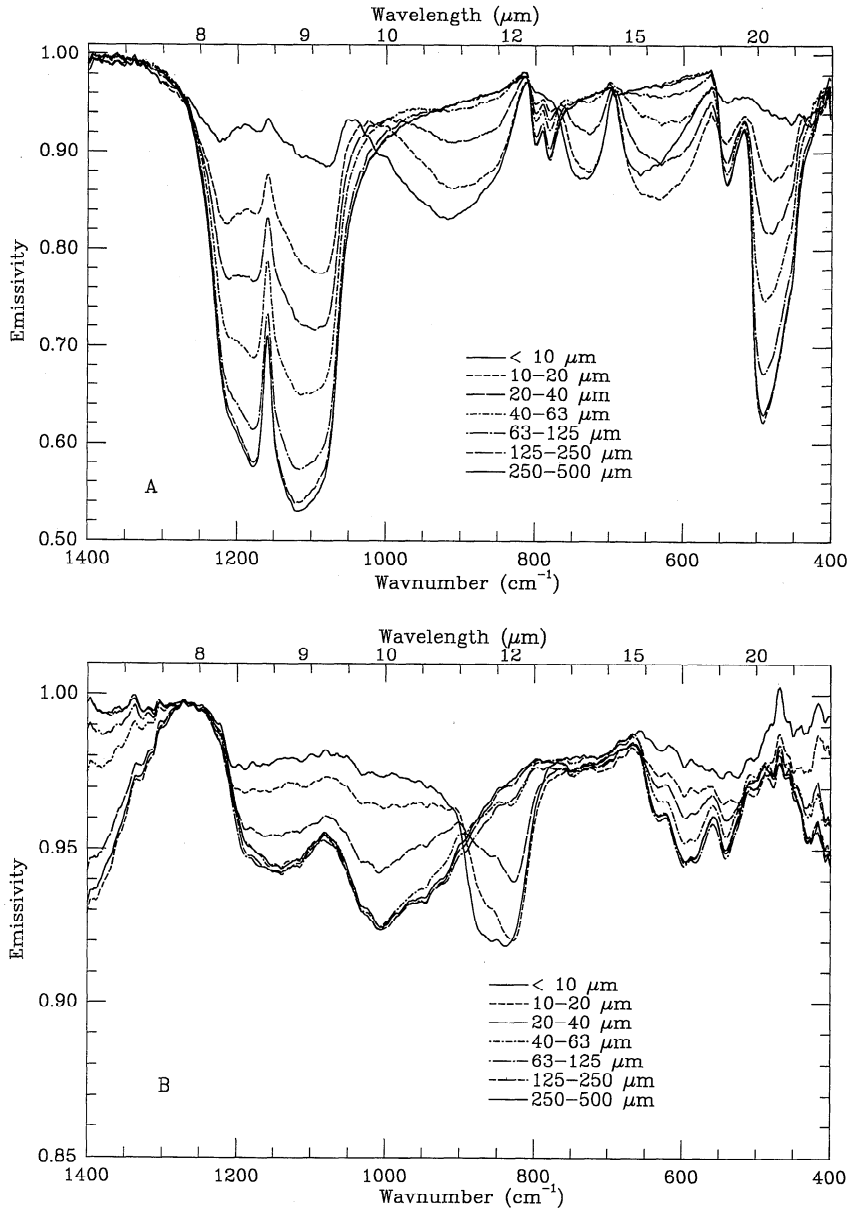

Figure 10. End-members of the binary mixing suite showing the effects of particle size reduction. Arranged from top to bottom from <10 μm to 250–500 μm. Note the Christiansen frequency (CF), which is invariant with particle size, at approximately 1400 cm^{-1} for quartz and 1260 cm^{-1} for andesine feldspar: (a) quartz and (b) andesine.

a function of size fraction. Using the one size end-member, the departure from linearity shown by the predicted model end-member percentage begins to occur below the 63–125 μm particle diameter. This departure is strongest for the 75:25 and weakest for the 25:75 quartz/andesine mixtures, respectively. The larger errors are a function of the strong absorption characteristics of quartz [*Thomson and Salisbury*, 1993].

In a remote sensing situation, where both the mineral type and potentially the grain diameter are unknown, constraints must be placed on the retrieval algorithm. The only independent piece of information that is returned from the algorithm is the root-mean-square error. Larger errors indicate poorer fits and may be used to disregard or accept the model's predicted percentage results. Figure 13 shows the variation of the RMS with particle size for deconvolution with both sets of sized end-members. The RMS of both end-member suites are virtually inseparable from 500 to 63 μm. However, at diameters less than this, there is a sharp increase in the RMS for the single size end-member deconvolution, whereas the errors remain approximately equal to 1.0×10^{-2} for the sized end-members. Obviously, these error values can not be universally applied to deconvolution results for different mixtures but do indicate the possibility of separating the effects of mineral type and grain diameter utilizing a retrieval algorithm.

5. Discussion

In general, the largest residual errors occur over the strongly absorbing portion of the emissivity spectrum. The deviation from the predicted result indicates that mixing of thermal energy for a multicomponent sample is slightly nonlinear in the regions of low emission. Large positive and negative residual

Table 9. Retrieval Model Results for Particle Size Variations Using the Same Diameter End-Members

End-Member Size Fraction, μm	Modeled Andesine, %	Modeled Quartz, %	Model Difference, %	RMS Error
	25:75 Quartz/Andesine Mix			
<10	85.65	14.12	10.65	8.662E−03
10–20	80.31	19.72	5.31	7.531E−03
20–40	75.24	24.87	0.24	7.130E−03
40–63	71.90	27.98	3.10	9.401E−03
63–125	79.61	20.33	4.61	6.262E−03
125–250	76.89	22.78	1.89	7.289E−03
250–500	78.65	21.04	3.65	5.694E−03
	50:50 Quartz/Andesine Mix			
<10	64.08	35.92	14.08	1.215E−02
10–20	55.92	44.08	5.92	1.089E−02
20–40	47.49	52.51	2.51	8.302E−03
40–63	48.79	51.21	1.21	7.202E−03
63–125	54.24	45.76	4.24	7.594E−03
125–250	49.88	50.12	0.12	9.036E−03
250–500	51.51	48.49	1.51	8.962E−03
	75:25 Quartz/Andesine Mix			
<10	36.30	63.70	11.30	1.264E−02
10–20	26.58	73.42	1.58	1.234E−02
20–40	18.37	81.63	6.63	7.633E−03
40–63	26.58	73.42	1.58	6.425E−03
63–125	27.04	72.96	2.04	8.075E−03
125–250	20.36	79.64	4.64	9.282E−03
250–500	26.48	73.52	1.48	9.822E−03

Read 8.662E−03 as 8.662×10^{-3}.

Table 10. Retrieval Model Results for Particle Size Variations Using the 255–500 μm End-Member

End-Member Size Fraction, μm	Modeled Andesine, %	Modeled Quartz, %	Model Difference, %	RMS Error
	25:75 Quartz/Andesine Mix			
<10	100.00	0.00	25.00	3.010E−02
10–20	100.00	0.00	25.00	2.889E−02
20–40	92.70	7.30	17.70	1.628E−02
40–63	81.90	18.10	6.90	1.119E−02
63–125	81.94	18.06	6.94	5.314E−03
125–250	77.01	22.99	2.01	7.401E−03
250–500	78.65	21.04	3.65	5.694E−03
	50:50 Quartz/Andesine Mix			
<10	100.00	0.00	50.00	2.527E−02
10–20	90.72	9.28	40.72	2.430E−02
20–40	77.60	22.40	27.60	1.316E−02
40–63	65.19	34.81	15.19	1.267E−02
63–125	58.93	41.07	8.93	7.141E−03
125–250	50.43	49.57	0.43	9.359E−03
250–500	51.51	48.49	1.51	8.962E−03
	75:25 Quartz/Andesine Mix			
<10	98.25	1.75	73.25	2.477E−02
10–20	79.73	20.27	54.73	2.471E−02
20–40	61.19	38.81	36.19	1.644E−02
40–63	49.00	51.00	24.00	1.307E−02
63–125	34.30	65.70	9.30	8.356E−03
125–250	21.34	78.66	3.66	9.795E−03
250–500	26.48	73.52	1.48	9.822E−03

Read 3.010E−02 as 3.010×10^{-2}.

errors are most noticeable at areas of high noise due to atmospheric water and over these largest mineral absorption bands (Figures 4 and 5). Discussed in detail by *Thomson and Salisbury* [1993], this slight nonlinearity is most clearly expressed in mixtures containing larger amounts of quartz (compare Figures 4a and 4c). Areas that show a positive residual error indicate more energy was emitted by the mineral mixture than the monomineralic end-members used to model the spectrum. This can be explained in terms of the wavelength dependent absorption coefficient of quartz. For example, at 1220 cm^{-1} (8.2 μm) quartz is weakly absorbing ($k \approx 1$) [*Salisbury and Wald*, 1992; *Moersch and Christensen*, 1995] and as seen in

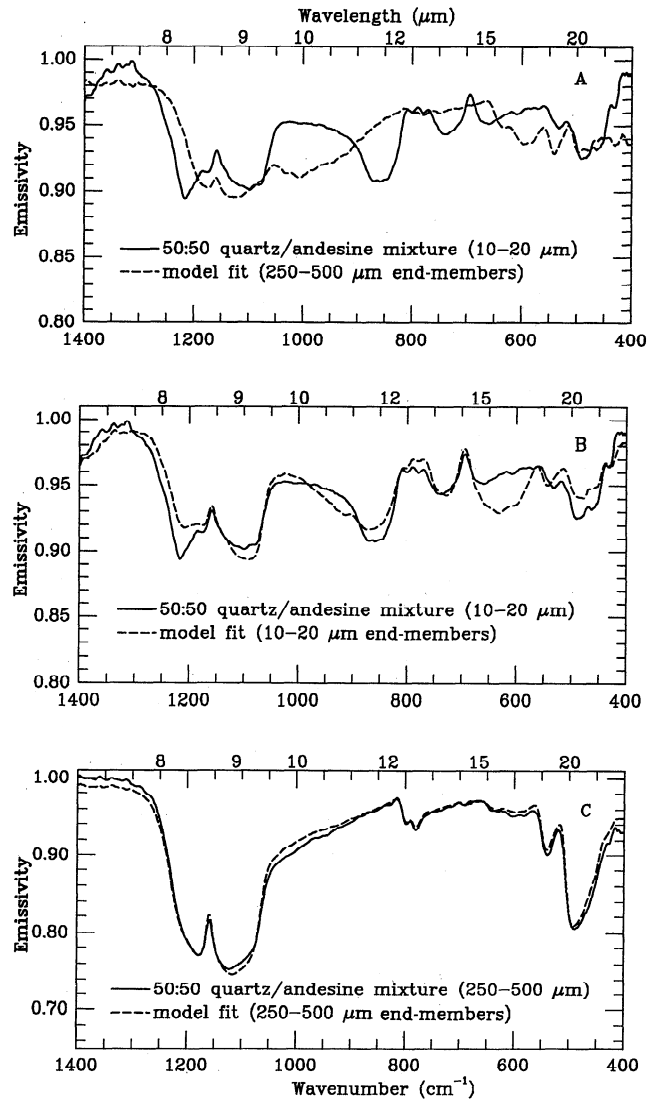

Figure 11. Emissivity spectra of the physical mixtures (solid) and the model fits (dashed) for the 50:50 quartz/andesine mixture using different size fraction end-members: (a) The 10–20 μm mixture using the 250–500 μm end-members. Note the regions of poor fit due to unmodeled features in the spectra of the fine-grained minerals. The results of the model are poor for this case (10:90%, RMS = 2.4%). (b) The same mixture described in Figure 11a using model end-members of the same size fraction (10–20 μm). Note the closer fit and more accurate results (44.4:55.6%, RMS = 1.1%). (c) Model fit for the 250–500 μm mixture using the same end-member size fraction. As expected, results are acceptable (48.5:51.5%, RMS = 0.9%).

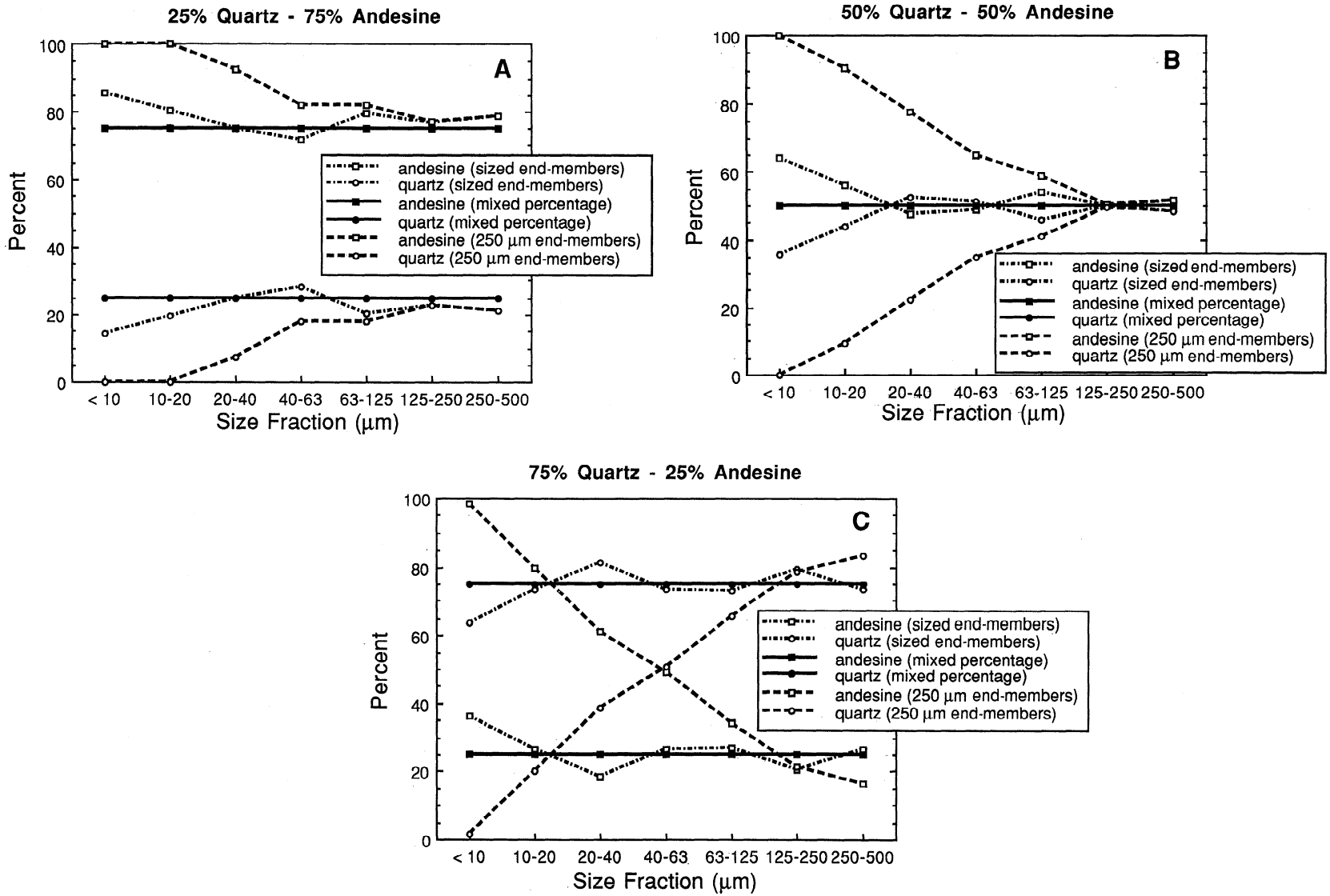

Figure 12. End-member-predicted percentages as a function of particle size for the binary mixing suite of quartz/andesine. The solid curve indicates the percentages formed in the physical mixtures; the dashed curves represent the attempted model fit using only the 250–500 μm end-members, whereas the dash-dotted curve shows the results using the same size end-member for the given mixture. The model begins to fail at ~60 μm using only the 250–500 μm end-members but remains valid until 10 μm with the use of multiple size fractions. At <10 μm, neither end-member fraction can reproduce the highly nonlinear mixing, and the model breaks down: (a) 25:75 quartz/andesine mixture, (b) 50:50 quartz/andesine mixture, and (c) 75:25 quartz/andesine mixture.

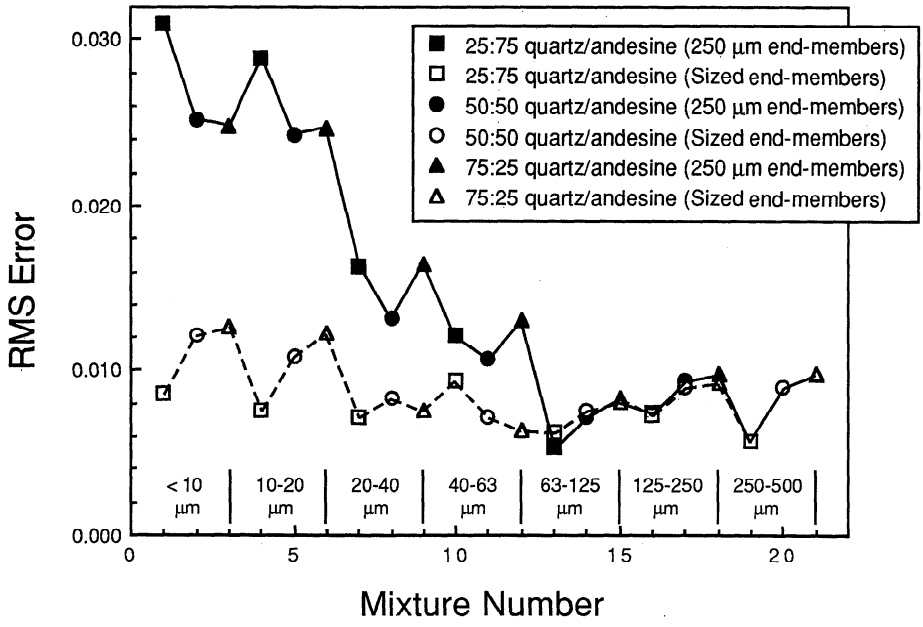

Figure 13. RMS error variation with grain size for the 21 mixtures described in Figures 11 and 12. The divergence of the RMS at approximately 60 μm is in accord with the higher errors in predicted mineral percentages and is caused by the appearance of spectral features due to volumetric scattering (see text). The solid curve shows the increased errors associated with trying to model these features with the 250–500 μm end-members. The dashed curve indicating a modeling attempt using the corresponding size fraction end-members, shows a much lower RMS error that remains nearly constant at 0.01.

Figure 4c, there is a <1% positive residual in the fit. In a sample consisting of only quartz grains (the end-member), emitted energy will undergo stronger surface reflections (i.e., lower emission) at this wavelength and have a lower component of volumetrically scattered energy. Where those quartz grains are mixed with other minerals, the same emitted energy will have a much greater chance of interacting with another grain with a different absorption coefficient. Those photons have a higher probability of reaching the detector after being reflected, thereby producing a shallower emission trough in the mixed spectrum.

At 1120 cm^{-1} (8.9 μm) the absorption coefficient of quartz increases ($k \approx 2$) [*Salisbury and Wald*, 1992; *Moersch and Christensen*, 1995], and the residual error becomes negative, indicating lower emission in the mixed spectrum. In this situation, the higher absorption of quartz promotes greater scattering at grain edges and surface asperities. This is intensified in a sample of quartz and produces a shallower emission trough. In the mixed sample, on the other hand, photons will tend to be reflected from grain surfaces by less absorbing minerals and thereby produce deeper emission features. These effects are most accentuated in regions where there is a strong contrast between end-member spectral features and in those minerals with very strong features. In mixtures of quartz, calcite, and enstatite this is compounded as both calcite and enstatite tend to be spectrally flat over the 1100–1200 cm^{-1} region and quartz has one of the most pronounced absorption bands of any mineral. However, even in this case, the residual errors are still less than 1% over these regions, and about 0.5% where averaged over the entire spectrum.

6. Conclusions

At thermal wavelengths, the physics of energy/matter interaction is significantly easier to model than in the VNIR and therefore is an ideal region for the application of a linear spectral retrieval approach. For this study a linear model was developed and extensively tested on laboratory thermal emission spectra of minerals for the first time. The results show that the assumption of linear mixing is valid and allows for the areal percentage of a mineral to be predicted to within a 4% average with less than 0.5% residual error. Other effects such as noise and instrument reproducibility were also examined and resulted in only minor errors of <4%. Figure 14 depicts this linearity for all the physical mixture suites used in this study. The data have an excellent linear regressive fit ($R^2 = 0.995$) and clearly show the accuracy of the technique. The results of the model for a wide range of silicate minerals as well as calcite proves its appropriateness for use in high spectral resolution studies of particulate mixtures. Further work is progressing on other mineral classes as well as whole rock analysis. In addition, the applicability to multispectral thermal infrared remote sensing data has been studied and is presented by *Ramsey* [1996] for several different regions.

The reduction in particle diameter caused a slightly greater increase in the model error. It was found that particle size effects could be modeled accurately down to the 63 μm size fraction using larger size end-members. Below this particle diameter, linear retrieval fails using a single size fraction for the end-member. However, with spectra of the appropriate size fraction, the errors are reduced significantly, with model success through the 10–20 μm range. This approach provides a much more straightforward and computationally quick method of deciphering complexly mixed spectra than does the use of radiative transfer models, which require the need for the absorption coefficients of every mineral. However, linear retrieval using the spectra of mineral size fractions is only an approximation and still clearly fails below 10 μm where nonlinear volume scattering dominates.

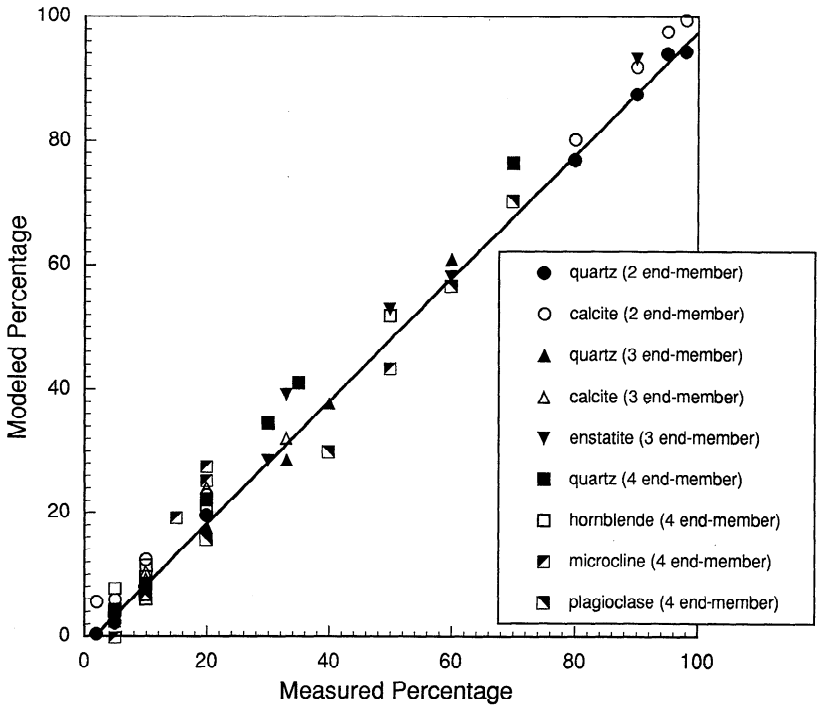

Figure 14. Model results for the entire set of physical mixtures (two-, three-, and four-component) described in the text. The accuracy of the model in all cases can be seen by the linear curve fit of the data points with a R^2 value of 0.995.

The viability and application of emission spectroscopy to remote sensing measurements of geologic surfaces are evident from the planned missions to Earth and Mars. The high data rate and large potential of overlapping information from instruments such as these has necessitated the need for fast, accurate, and innovative processing tools such as linear deconvolution. As has happened for most of remote sensing history, techniques are quick to develop and even quicker to be discarded as the next innovation is unveiled. It is critical, however, to understand the physics of thermal emission and how it is effected by numerous complexities inherent upon the mixing of radiant energy.

Acknowledgments. The authors wish to thank Douglas Howard for his assistance with sample preparation. Mark Mann and Dale Noss also added to this work through countless discussions on FORTRAN and C programming. The quality of this manuscript was greatly improved thanks to helpful reviews by David Crown, Steven Mackwell, and John Mustard. Research funding for this study has been provided by NASA through the Planetary Geology and Geophysics Program as well as the Mission to Planet Earth, ASTER science project.

References

Adams, J. B., M. O. Smith, and P. E. Johnson, Spectral mixture modeling: A new analysis of rock and soil types at the Viking Lander I site, *J. Geophys. Res.*, *91*, 8098–8112, 1986.

Adams, J. B., M. O. Smith, and A. R. Gillespie, Simple models for complex natural surfaces: A strategy for the hyperspectral era of remote sensing, *Proc. IGARSS Can. Symp. Remote Sens., 12th*, 16–21, 1989.

Adams, J. B., M. O. Smith, and A. R. Gillespie, Imaging spectroscopy: Interpretation based on spectral mixture analysis, in *Remote Geochemical Analysis: Elemental and Mineralogical Composition*, edited by C. M. Pieters and P. A. Englert, pp. 145–166, Cambridge Univ. Press, New York, 1993.

Adams, J. B., D. E. Sabol, V. Kapos, R. A. Filho, D. A. Roberts, M. O. Smith, and A. R. Gillespie, Classification of multispectral images based on fractions of end-members: Application to land-cover change in the Brazilian Amazon, *Remote Sens. Environ.*, *52*, 137–154, 1995.

Barbera, P. W., Geology of the Kelso-Baker Region, Mohave Desert, California using thermal infrared multispectral scanner data, M.S. thesis, 198 pp., Ariz. State Univ., Tempe, 1989.

Blount, G., M. O. Smith, J. B. Adams, R. Greeley, and P. R. Christensen, Regional aeolian dynamics and sand mixing in the Gran Desierto: Evidence from Landsat Thematic Mapper images, *J. Geophys. Res.*, *95*, 15,463–15,482, 1990.

Christensen, P. R., Eolian intracrater deposits on Mars: Physical properties and global distribution, *Icarus*, *56*, 496–518, 1983.

Christensen, P. R., Regional dust deposits on Mars: Physical properties, age, and history, *J. Geophys. Res.*, *91*, 3533–3545, 1986.

Christensen, P. R., and S. T. Harrison, Thermal-infrared emission spectroscopy of natural surfaces: Application to desert varnish coatings on rocks, *J. Geophys. Res.*, *98*, 19,819–19,834, 1993.

Christensen, P. R., H. H. Kieffer, S. C. Chase, and D. D. Laporte, A thermal emission spectrometer for identification of surface composition from Earth orbit, in *Commercial Applications and Scientific Research Requirements for Thermal Infrared Observations of Terrestrial Surfaces, NASA-EOSAT Joint Report*, pp. 119–132, Earth Obs. Satell. Co., Lanham, Md., 1986.

Christensen, P. R., D. L. Anderson, S. C. Chase, R. N. Clark, H. H. Kieffer, M. C. Malin, J. C. Pearl, J. Carpenter, N. Bandeira, F. G. Brown, and S. Silverman, Thermal emission spectrometer experiment: The Mars observer mission, *J. Geophys. Res.*, *97*, 7719–7734, 1992.

Clark, R. N., Spectral properties of mixtures of montmorillonite and dark carbon grains: Implications for remote sensing minerals containing chemically and physically adsorbed water, *J. Geophys. Res.*, *88*, 10,635–10,644, 1983.

Crown, D. A., and C. M. Pieters, Spectral properties of plagioclase and pyroxene mixtures and the interpretation of lunar soil spectra, *Icarus*, *72*, 492–506, 1987.

Dixon, J. C., Aridic soils, patterned ground, and desert pavements, in *Geomorphology of Desert Environments*, edited by A. D. Abrahams and A. J. Parsons, pp. 64–81, Chapman and Hall, New York, 1994.

Dozier, J., A method for satellite identification of surface temperature

fields of subpixel identification, *Remote Sens. Environ.*, *11*, 221–229, 1981.
Eastes, J. W., Spectral properties of halite-rich mineral mixtures: Implications for middle infrared remote sensing of highly saline environments, *Remote Sens. Environ.*, *27*, 289–304, 1989.
Gillespie, A. R., Spectral mixture analysis of multispectral thermal infrared images, *Remote Sens. Environ.*, *42*, 137–145, 1992.
Gillespie, A. R., M. O. Smith, J. B. Adams, and S. C. Willis, Spectral mixture analysis of multispectral thermal infrared images, in *Proceedings of the Second Annual Airborne Earth Science Workshop*, vol. 2, edited by E. A. Abbott, *JPL Publ.*, *90-55*, 57–74, 1990.
Hamilton, V. E., P. R. Christensen, and H. Y. McSween Jr., Determination of Martian meteorite lithologies and mineralogies using vibrational spectroscopy, *J. Geophys. Res.*, *102*, 25,593–25,603, 1997.
Hapke, B., Bidirectional reflectance spectroscopy, 1, Theory, *J. Geophys. Res.*, *86*, 3039–3054, 1981.
Hapke, B., *Theory of Reflectance and Emittance Spectroscopy*, Cambridge Univ. Press, New York, 1993.
Harden, D. R., N. E. Biggar, and M. L. Gillam, Quaternary deposits and soils in and around Spanish Valley, Utah, *Spec. Pap. Geol. Soc. Am.*, *203*, 43–64, 1985.
Hunt, G. R., Infrared spectral behavior of fine particulate solids, *J. Phys. Chem.*, *80*, 1195–1198, 1976.
Hunt, G. R., and R. K. Vincent, The behavior of spectral features in the infrared emission from particulate surfaces of various grain sizes, *J. Geophys. Res.*, *73*, 6039–6046, 1968.
Johnson, P. E., M. O. Smith, S. Taylor-George, and J. B. Adams, A semiempirical method for analysis of the reflectance spectra of binary mineral mixtures, *J. Geophys. Res.*, *88*, 3557–3561, 1983.
Johnson, P. E., M. O. Smith, and J. B. Adams, Simple algorithms for remote determination of mineral abundances and particle sizes from reflectance spectra, *J. Geophys. Res.*, *97*, 2649–2657, 1992.
Kahle, A. B., F. D. Palluconi, S. J. Hook, V. J. Realmuto, and G. Bothwell, The advanced spaceborne thermal emission and reflectance radiometer (ASTER), *Int. J. Imaging Syst. Technol.*, *3*, 144–156, 1991.
Lyon, R. J. P., Evaluation of infrared spectrophotometry for compositional analysis of lunar and planetary soils, II, Rough and powdered surfaces, *NASA Contract Rep.*, *CR-100*, 1964.
Lyon, R. J. P., Analysis of rocks by spectral infrared emission (8 to 25 microns), *Econ. Geol.*, *60*, 715–736, 1965.
Moersch, J. E., Modelling particle size effects on the thermal emission spectra of minerals in the thermal infrared, M.S. thesis, 77 pp., Ariz. State Univ., Tempe, 1992.
Moersch, J. E., and P. R. Christensen, Thermal emission from particulate surfaces: A comparison of scattering models with measured spectra, *J. Geophys. Res.*, *100*, 7465–7477, 1995.
Mustard, J. F., Relationships of soil, grass, and bedrock over the Kaweah Serpentine Melange through spectral mixture analysis of AVIRIS data, *Remote Sens. Environ.*, *44*, 293–308, 1993.
Mustard, J. F., and J. E. Hays, Effects of hyperfine particles on reflectance spectra from 0.3 to 25 μm, *Icarus*, *125*, 145–163, 1997.
Mustard, J. F., and C. M. Pieters, Photometric phase functions of common geologic minerals and applications to quantitative analysis of mineral mixture reflectance spectra, *J. Geophys. Res.*, *94*, 13,619–13,634, 1989.
Nash, D. B., and J. E. Conel, Spectral reflectance systematics for mixtures of powdered hypersthene, labradorite, and ilmenite, *J. Geophys. Res.*, *79*, 1615–1621, 1974.
Palluconi, F. D., and H. H. Kieffer, Thermal inertia mapping of Mars from 60°S to 60°N, *Icarus*, *45*, 415–426, 1981.
Press, W. H., B. P. Flannery, S. A. Teukolsky, and W. T. Vetterling, *Numerical Recipes in C: The Art of Scientific Computing*, 1st ed., pp. 517–539, Cambridge Univ. Press, New York, 1988.
Ramsey, M. S., Quantitative analysis of geological surfaces: A deconvolution algorithm for midinfrared remote sensing data, Ph.D. dissertation, 276 pp., Ariz. State Univ., Tempe, 1996.
Ramsey, M. S., and P. R. Christensen, The linear 'un-mixing' of laboratory infrared spectra: Implications for the thermal emission spectrometer (TES) experiment, Mars Observer (abstract), *Lunar Planet. Sci., XXIII*, 1127–1128, 1992.
Ramsey, M. S., D. A. Howard, P. R. Christensen, and N. Lancaster, Mineralogic variability of the Kelso Dunes, Mojave Desert, California derived from thermal infrared multispectral scanner (TIMS) data, in *Summaries of the Fourth Annual Airborne Earth Science Workshop*, vol. 2, edited by V. J. Realmuto, *JPL Publ.*, *93-26*, 9–12, 1993.
Roberts, D. A., M. O. Smith, J. B. Adams, D. E. Sabol, A. R. Gillespie, and S. C. Willis, Isolating woody plant material and senescent vegetation from green vegetation in AVIRIS data, in *Proceedings of the Second Annual Airborne Earth Science Workshop*, vol. 1, edited by R. A. Green, *JPL Publ.*, *90-54*, 42–57, 1990.
Ruff, S., P. R. Christensen, P. W. Barbera, and D. L. Anderson, Quantitative thermal emission spectroscopy of minerals: A laboratory technique for measurement and calibration, *J. Geophys. Res.*, *102*, 14,899–14,913, 1997.
Sabol, D. E., J. B. Adams, and M. O. Smith, Quantitative subpixel spectral detection of targets in multispectral images, *J. Geophys. Res.*, *97*, 2659–2672, 1992.
Salisbury, J. W., Mid-infrared spectroscopy: Laboratory data, in *Remote Geochemical Analysis: Elemental and Mineralogical Composition*, edited by C. M. Pieters and P. A. Englert, pp. 79–98, Cambridge Univ. Press, New York, 1993.
Salisbury, J. W., and A. Wald, The role of volume scattering in reducing spectral contrast of reststrahlen bands in spectra of powdered minerals, *Icarus*, *96*, 121–128, 1992.
Salisbury, J. W., A. Wald, and D. M. D'Aria, Thermal-infrared remote and Kirchoff's law, 1, Laboratory measurements, *J. Geophys. Res.*, *99*, 11,897–11,911, 1994.
Singer, R. B., Near-infrared spectral reflectance of mineral mixtures: Systematic combinations of pyroxenes, olivine, and iron oxides, *J. Geophys. Res.*, *86*, 7967–7982, 1981.
Singer, R. B., and T. B. McCord, Mars: Large scale mixing of bright and dark surface materials and implications for analysis of spectral reflectance, *Proc. Lunar Planet. Sci. Conf.*, *10th*, 1835–1848, 1979.
Thomson, J. L., and J. W. Salisbury, The mid-infrared reflectance of mineral mixtures (7–14 μm), *Remote Sens. Environ.*, *45*, 1–13, 1993.
Tompkins, S., J. F. Mustard, C. M. Pieters, and D. W. Forsyth, Optimization of end-members for spectral mixture analysis, *Remote Sens. Environ.*, *59*, 472–489, 1997.
Wald, A. E., Modeling thermal infrared (2–14 μm) reflectance spectra of frost and snow, *J. Geophys. Res.*, *99*, 24,241–24,250, 1994.
Wald, A. E., and J. W. Salisbury, Thermal infrared directional emissivity of quartz, *J. Geophys. Res.*, *100*, 24,665–24,675, 1995.

P. R. Christensen and M. S. Ramsey, Department of Geology, Box 871404, Arizona State University, Tempe, AZ 85287-1790. (e-mail: ramsey@elwood.la.asu.edu)

(Received February 25, 1997; revised August 28, 1997;
accepted September 29, 1997.)